T-3905

EFFECTS OF LATTICE MISMATCH ON THE PHOTOVOLTAIC PERFORMANCE OF $GaAs_{0.74}P_{0.26}$ SHALLOW HOMOJUNCTIONS

Mark W. Wanlass

ARTHUR LAKES LIBRARY
COLORADO SCHOOL OF MINES
GOLDEN, CO 80401

ProQuest Number: 10783616

All rights reserved

INFORMATION TO ALL USERS
The quality of this reproduction is dependent upon the quality of the copy submitted.

In the unlikely event that the author did not send a complete manuscript
and there are missing pages, these will be noted. Also, if material had to be removed,
a note will indicate the deletion.

ProQuest 10783616

Published by ProQuest LLC (2018). Copyright of the Dissertation is held by the Author.

All rights reserved.
This work is protected against unauthorized copying under Title 17, United States Code
Microform Edition © ProQuest LLC.

ProQuest LLC.
789 East Eisenhower Parkway
P.O. Box 1346
Ann Arbor, MI 48106 – 1346

T-3905

A thesis submitted to the Faculty and the Board of Trustees of the Colorado School of Mines in partial fulfillment of the requirements for the degree of Master of Science (Physics).

Golden, Colorado

Date 4/11/90

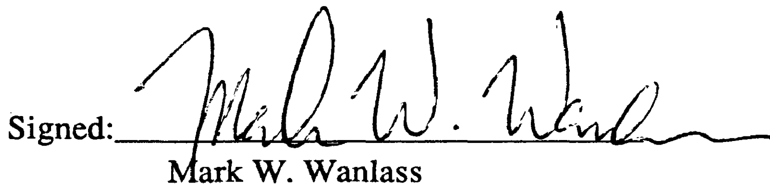

Signed:
Mark W. Wanlass

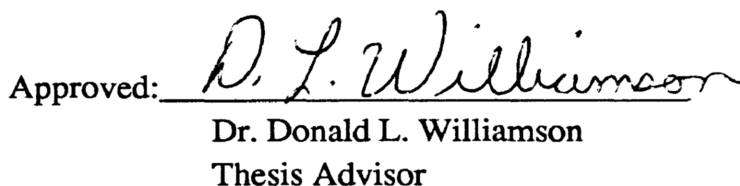

Approved:
Dr. Donald L. Williamson
Thesis Advisor

Golden, Colorado

Date 4/12/90

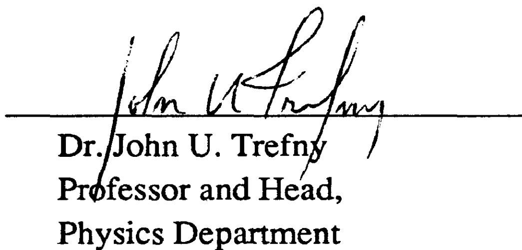

Dr. John U. Trefny
Professor and Head,
Physics Department

ABSTRACT

An empirical assessment of the effects of lattice mismatch on the photovoltaic performance of $GaAs_{0.74}P_{0.26}$ shallow-homojunction solar cells is presented. The motivation for studying the lattice mismatch problem is discussed in terms of its relevance to the development of high-performance tandem solar cells.

A compositionally graded $GaAs_{1-x}P_x$/GaAs heterostructure epitaxially grown by atmospheric-pressure metalorganic vapor phase epitaxy (APMOVPE) is employed as a means of studying the lattice mismatch problem in a controlled and systematic manner. The structure is used to prepare a set of nominally identical $GaAs_{0.74}P_{0.26}$ shallow-homojunction solar cells with dislocation densities and morphologies which vary over a wide range. Several analytical techniques are used to establish correlations between the grading parameters, defect type, density and morphology, surface morphology and the solar cell performance and electrical characteristics.

The most salient observations and conclusions resulting from this study include:

1) Thin compositional grades can be used effectively in the $GaAs_{0.74}P_{0.26}$/GaAs system to produce high-performance $GaAs_{0.74}P_{0.26}$ solar cells which are free of microcracks.

2) A catastrophic degradation in solar cell performance occurs when extensive misfit dislocation networks are present in the active solar cell layers. Such networks must be eliminated in order to achieve high energy conversion efficiencies. This is achieved through an appropriate choice of the grading parameters.

3) For solar cells with only threading dislocations present in the active layers, it is found that threading dislocation densities less than $5x10^5$ cm^{-2} do not significantly degrade the solar cell performance at one-sun illumination intensity. Moreover, under these

circumstances the predominant power-loss mechanism is a reduction of the short-circuit current density through recombination of photogenerated carriers at the threading dislocations. Based on a differential analysis of short-circuit current density *vs* threading dislocation density data, the effective recombination radius of a threading dislocation is determined to be 1.3 μm.

4) Strong correlations are observed between the grading parameters, dislocation type and density, surface morphology and solar cell characteristics. Finely cross-hatched surfaces are associated with cell layers that have only threading dislocations present. A rough, irregular surface morphology indicates the presence of a dense, extensive misfit dislocation network within a few microns of the surface. Furthermore, the transition from a finely cross-hatched morphology to a rough, irregular surface coincides with a catastrophic decrease in the observed solar cell performance. Therefore, a qualitative measure of the effectiveness of a particular compositional grade can be gained by simply observing the surface morphology. This purely empirical result may be useful for determining the appropriate design parameters for a compositional grade in an arbitrary lattice-mismatched III-V system where little is known about the material properties.

Suggestions for further work in this area are also discussed.

TABLE OF CONTENTS

	Page
ABSTRACT	iii
LIST OF FIGURES	vii
LIST OF TABLES	x
LIST OF SYMBOLS	xi
ACKNOWLEDGEMENTS	xiv
1.0 INTRODUCTION	1
1.1 Multijunction Solar Cells and the Lattice Mismatch Problem	1
1.2 Project Concept, Scope and Objectives	6
2.0 TECHNICAL BACKGROUND	12
2.1 Introduction	12
2.2 $GaAs_{1-x}P_x$/GaAs Epitaxial Heterostructures	12
2.2.1 Properties of $GaAs_{1-x}P_x$	12
2.2.2 Defects in $GaAs_{1-x}P_x$/GaAs Heterostructures	16
2.3 Photovoltaic Device Performance Theory	18
2.3.1 Device Performance Parameters	18
2.3.2 Anticipated Effects of Defects On Device Performance	23
3.0 EXPERIMENTAL PROCEDURE	26
3.1 Introduction	26
3.2 Growth of $GaAs_{1-x}P_x$/GaAs Heterostructures by APMOVPE	26
3.2.1 General Description of APMOVPE	26
3.2.2 APMOVPE Apparatus and Source Materials	31
3.2.3 Epitaxial Growth Procedure	38
3.3 $GaAs_{0.74}P_{0.26}$ Solar Cell Fabrication	43
3.4 Material/Device Characterization	45
4.0 RESULTS AND DISCUSSION	49
4.1 Introduction	49
4.2 Properties of $GaAs_{1-x}P_x$/GaAs Epitaxial Device Structures	49
4.2.1 Morphology of Surfaces and Interfaces	49

4.2.2 Compositional Analysis 54
4.2.3 Defect Analysis 61
4.3 $GaAs_{0.74}P_{0.26}$ Photovoltaic Device Characteristics 70
4.3.1 Illuminated J-V Characteristics 70
4.3.2 Absolute External Quantum Efficiency 76
4.3.3 Dark J-V Characteristics 79

5.0 CONCLUSIONS AND SUGGESTIONS FOR FURTHER WORK 83

REFERENCES 86

LIST OF FIGURES

		Page
Figure 1.1	Configurations for two-junction tandem solar cells.	3
Figure 1.2	Bandgap *vs* Lattice Parameter for the III-V family of semiconductors at 300 K. The coordinates for Si and Ge are also included.	4
Figure 1.3	A schematic cross section of the compositionally graded $GaAs_{1-x}P_x$/GaAs heterostructure used to produce $GaAs_{0.74}P_{0.26}$ shallow homojunctions with varying defect densities.	7
Figure 2.1	Energy Gap *vs* x for $GaAs_{1-x}P_x$ at 300 K. The dotted lines indicate the average composition (x = 0.26) and energy gap (E_g = 1.74 eV) for the devices used in this study.	15
Figure 2.2	Illuminated and dark J-V characteristics for an ideal solar cell. The power output is given by the dashed curve.	21
Figure 2.3	(a) Simplifed equivalent circuit for a solar cell with finite shunt resistance R_{sh}. (b) The effect of shunt resistance on the I-V characteristic of an ideal solar cell by graphical construction.	25
Figure 3.1	A schematic diagram of the APMOVPE gas handling system.	33
Figure 3.2	Diagrams of the APMOVPE reactor vessel, including: (a) A side view of the complete reactor vessel revealing the gas flow pattern and major components. (b) A top view of the specially designed reactor vessel inlet. (c) A top view through a section directly above the susceptor showing the gas flow pattern. (d) An oblique view of the reactor vessel top.	36
Figure 3.3	Typical thickness profiles for $GaAs_{1-x}P_x$ epilayers grown on 2cm x 2cm GaAs substrates.	39

Figure 3.4	EPMA surface composition profile for a typical $GaAs_{0.74}P_{0.26}$ epilayer.	40
Figure 3.5	Photomicrograph of a finished $GaAs_{0.74}P_{0.26}$ solar cell array fabricated on a GaAs wafer, as viewed from above. The front grid contacts and individual device mesas are visible.	46
Figure 4.1	Photomicrographs of six different compositionally graded $GaAs_{1-x}P_x$/GaAs heterostructure cross sections, with the grading parameters for each listed below.	52
Figure 4.2	Photomicrographs of surface morphology as a function of the grading parameters.	53
Figure 4.3	Photomicrographs of growth defects observed on the surface of sample 3 (n = 7, t = 8 μm) shown at (a) low and(b) high magnification.	55
Figure 4.4	EPMA cross sectional composition profile for a continously graded $GaAs_{1-x}P_x$/GaAs heterostructure (sample 1, continuous, t = 8 μm).	58
Figure 4.5	EPMA cross sectional composition profile for a step graded $GaAs_{1-x}P_x$/GaAs heterostructure (sample 7, n = 3, t = 8 μm).	59
Figure 4.6	$x_s/(1-x_s)$ *vs* (PH_3 flow rate)/(AsH_3 flow rate) , showing a least-squares fit to the experimental data. The slope of the line gives the P vapor/solid distribution coefficient K_p.	64
Figure 4.7	x_s *vs* x_v for $GaAs_{1-x}P_x$ epilayers grown under the conditions used in this study. The solid line fit was obtained using the empirically derived P vapor/solid distribution coefficient (K_p = 0.395).	65
Figure 4.8	Cross sectional TEM montage of a compositionally step graded $GaAs_{1-x}P_x$ structure revealing dislocation networks in the vicinity of each compositional step.	67

Figure 4.9 Plan-view EBIC micrographs revealing the dislocation density and morphology as a function of the grading parameters. The dark lines and spots correspond to dislocations where photogenerated minority carriers recombine. 69

Figure 4.10 Typical J-V characteristics under standard 1-sun illumination for $GaAs_{0.74}P_{0.26}/GaAs$ SHJ solar cells (no ARC) having the five different compositionally graded structures listed. 74

Figure 4.11 AEQE vs Wavelength data (no ARC) for $GaAs_{0.74}P_{0.26}/GaAs$ SHJ solar cells having the five different compositional grades listed. 77

Figure 4.12 Typical forward-biased J-V characteristics in the dark for $Ga_{0.74}P_{0.26}/GaAs$ SHJ solar cells with five different compositional grades. 80

Figure 4.13 Typical reverse-biased J-V characteristics in the dark for $GaAs_{0.74}P_{0.26}/GaAs$ SHJ solar cells with five different compositional grades. 82

LIST OF TABLES

Page

Table 3.1 Chemical reactants used in the APMOVPE process. 34

Table 3.2 APMOVPE growth conditions and reactor performance characteristics for $GaAs_{1-x}P_x$/GaAs epitaxial heterostructures. 42

Table 3.3 Material/device characterization techniques used to investigate the $GaAs_{1-x}P_x$/GaAs device structures. 47

Table 4.1 Characteristics of the compositional in each of the $GaAs_{1-x}P_x$/GaAs epitaxial structures. 50

Table 4.2 EPMA device layer compositional data summary for all $GaAs_{1-x}P_x$ samples grown in this study. 56

Table 4.3 A summary of the vapor/solid compositional data used to determine x_s *vs* x_v. The parameters used to calculate the empirical P vapor/solid distribution coefficient K_p are also listed. 62

Table 4.4 A summary of the illuminated J-V solar cell performance parameters for $GaAs_{0.74}P_{0.26}$ SHJ cells (no ARC) as a function of the dislocation type and density in the device layers, and the grading structure. The figures in parentheses indicate the range of values observed on each device wafer. 71

LIST OF SYMBOLS

Symbol	Description
a	Lattice parameter.
a_e	Lattice parameter of epitaxial layer.
a_s	Lattice parameter of substrate.
α	Optical absorption coefficient.
c	Speed of light.
d	Depth into semiconductor measured from surface.
D_M	Lineal density of misfit dislocations.
D_T	Areal density of threading dislocations.
Δt_{st}	Thickness of layers between compositional steps in a step grade.
Δx_{st}	Incremental change in the P mole fraction at a compositional step.
η	Photovoltaic energy conversion efficiency.
E	Energy.
E_g	Semiconductor energy gap or bandgap.
f	Flow rate.
F	Junction ideality factor.
FF	Fill factor.

G	P mole fraction gradient in a continuously graded $GaAs_{1-x}P_x$ layer.
Γ	Photon flux.
Γ_0	Incident photon flux.
h	Planck constant.
I	Electrical current.
I_D	Diode current.
I_L	Light current.
I_{LOAD}	Load current.
J	Electrical current density.
J_L	Photocurrent density.
J_{sc}	Short-circuit current density.
J_0	Reverse-saturation current density (injection).
J_{00}	Effective reverse-saturation current density (injection/recombination).
k	Boltzmann constant.
K_P	P vapor/solid distribution coefficient.
λ	Wavelength.
n	Number of compositional steps.
P	Power.

P_i	Incident areal solar power density.
P_m	Maximum areal power density.
P_{MO}	Metalorganic source vapor pressure.
P_0	Ambient atmospheric pressure.
q	Electronic charge.
R_{LOAD}	Load resistance.
R_{sh}	Shunt resistance.
t_{GL}	Total thickness of compositionally graded layer.
T	Temperature.
T_g	Epitaxial growth temperature.
V	Voltage.
V_{oc}	Open-circuit voltage.
x	Mole fraction of P in $GaAs_{1-x}P_x$.
x_c	Direct-indirect bandgap crossover P mole fraction for $GaAs_{1-x}P_x$.
x_s	Mole fraction of P in the growing $GaAs_{1-x}P_x$ epitaxial layer.
x_{sc}	Mole fraction of P in the solar cell junction layers.
x_v	Mole fraction of P in the nutrient vapor.

ACKNOWLEDGEMENTS

I would like to express my thanks and appreciation to a number of individuals who have contributed to the completion of this thesis. Additionally, I am grateful to the Solar Energy Research Institute (SERI) for providing me with the opportunity of performing the research required for the thesis while being a full-time employee.

Special thanks are due to my thesis advisor Dr. Don Williamson for his guidance and patience. His flexibility allowed me to complete this work while working full-time at SERI. I would also like to thank Dr. John Trefny (CSM), Dr. Larry Kazmerski (SERI) and Dr. Mowafak Al-Jassim (SERI) for serving as thesis committee members.

Dr. Tim Coutts, my immediate supervisor at SERI over the last five years, has provided special leadership and inspiration. I thank him for his persistence in urging me to complete this work and for providing the opportunity to continue my career in III-V materials and devices.

I am grateful to several of my colleagues at SERI who have contributed to the results presented herein. They are listed below along with the area in which they contributed.

Dr. Mowafak Al-Jassim: Plan-view EBIC, TEM and helpful discussions.
Keith Emery: IJV data, DJV data, assistance in data reduction and helpful discussions.
Tim Gessert: Device processing.
Chuck Herrington: EPMA data.
Kim Jones: TEM.
Alice Mason: Plan-view EBIC.
Rick Matson: Plan-view EBIC.
Carl Osterwald: Spectral response data.

1.0 INTRODUCTION

1.1 Multijunction Solar Cells and the Lattice Mismatch Problem

The realization of large-scale, cost-effective photovoltaic power generation will depend upon reducing the cost and increasing the energy conversion efficiency of photovoltaic systems. A promising pathway toward achieving conversion efficiencies far exceeding those possible with single-junction solar cells involves the development of high-performance multijunction cells. During the last ten years, multijunction solar cells have been the subject of numerous theoretical and experimental investigations which have clearly demonstrated the potential of such devices. However, despite the potential for high efficiencies, progress in this area of research has been hampered by several practical problems, including: 1) difficulties in the development of a wide range of high-quality epitaxial semiconductor materials, and 2) the deleterious effects of lattice parameter mismatch on the performance of solar cells. It is the purpose of this thesis to investigate the details of the lattice mismatch problem and its effects on photovoltaic performance.

Multijunction or tandem solar cells consist of a number of individual single-junction cells (subcells) with different energy gaps stacked in optical series with the bandgaps arranged from highest to lowest, top to bottom. The tandem cell concept was first described by Jackson [1] in 1955 as a means of improving photovoltaic conversion efficiency. Such an arrangement results in an optical cascade effect which, if properly designed, allows each subcell in the stack to absorb a portion of the solar spectrum over which it can efficiently convert light energy to electrical energy. Thus, a high overall efficiency for the stacked cell system is achieved. In principal, a multijunction cell may contain any number of junctions, however, a practical limit of two or three is usually considered since the complexity of the tandem

structure increases substantially as the number of junctions is increased, while the marginal increase in efficiency drops off rapidly. Several possible configurations are available for tandem cells depending upon the desired method of stacking, and extracting power from, the individual subcells. Examples of these for a two-junction system are given in Figure 1.1 showing the two-terminal monolithic, three-terminal monolithic and four-terminal mechanically stacked configurations. Each of the tandem options has its own advantages and drawbacks in terms of fabrication and performance. The principal design considerations for tandem cells include choice of bandgaps for each of the subcells and, traditionally, for the monolithically configured cells, matching the lattice constants of the semiconductor alloys used in the stack. Recent modeling calculations for two-junction tandem cells indicate that the optimum bandgaps for the top and bottom cells lie in the ranges 1.3 - 2.0 eV and 0.65 - 1.2 eV, respectively, depending upon the application and operating conditions [2].

Single-crystal III-V semiconductor alloys are an attractive materials choice for tandem cell fabrication since they offer bandgap/lattice parameter tunability and suitable electrical and optoelectronic characteristics. Several III-V alloys are available with direct bandgaps in the optimum ranges mentioned previously for the top and bottom cells. The variation of bandgap with lattice parameter for the III-V materials system is shown in Figure 1.2 along with the coordinates for the important Group IV semiconductors silicon and germanium. It is evident that numerous possibilities exist for combining alloys with the proper bandgaps for optimum tandem cell performance. However, not all alloys are easily synthesized by present methods and to date only a limited number have been produced which exhibit acceptable electronic and optoelectronic properties. Furthermore, for two-junction tandem cell applications few alloy pairs exist with the proper bandgap values, matching lattice parameters and which are lattice matched to commercially available single-crystal substrates (e.g., Si, Ge, GaAs, InP, etc.). Therefore, within the constraints imposed by considering only optimally

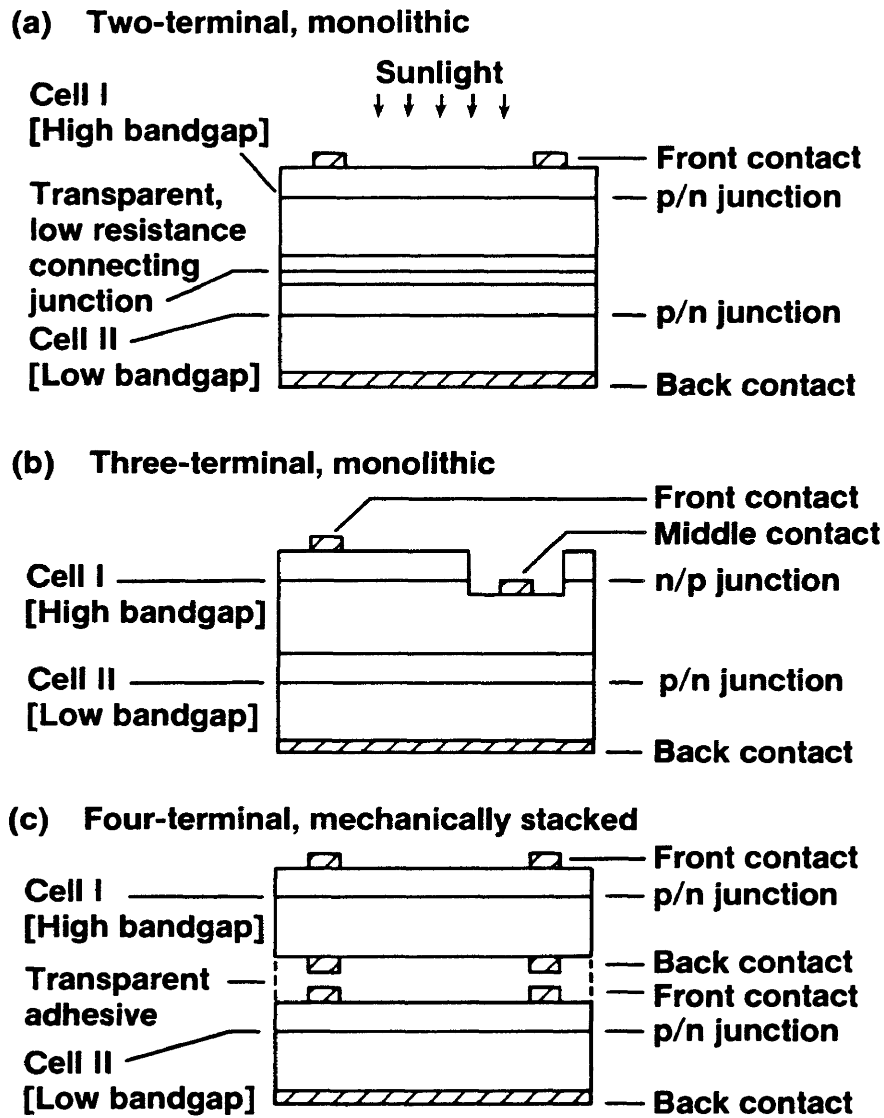

Figure 1.1 Configurations for two-junction tandem solar cells.

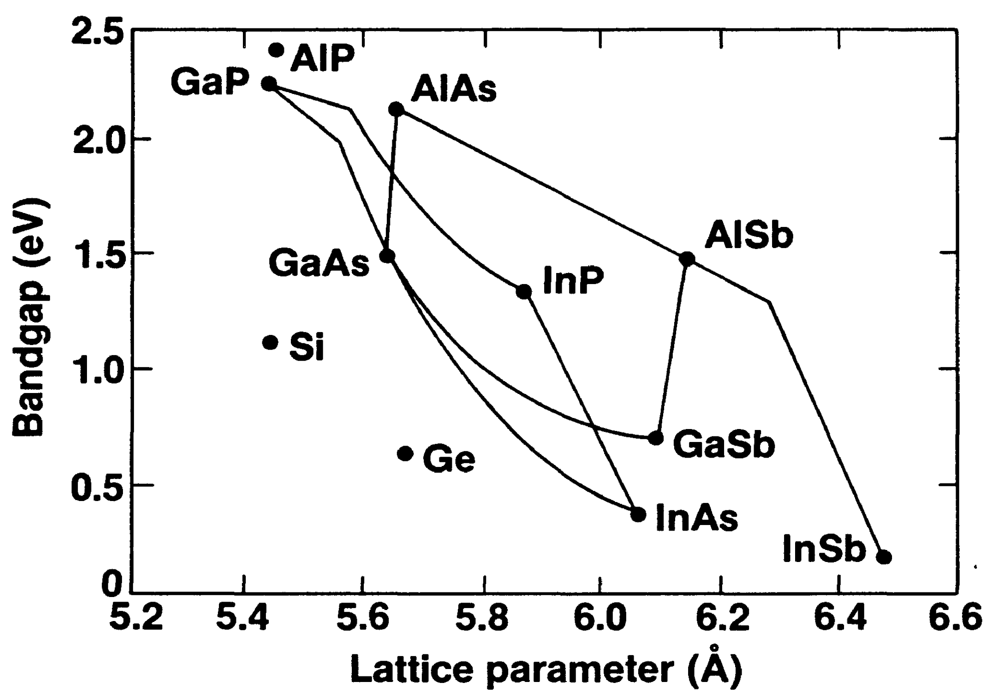

Figure 1.2 Bandgap *vs* Lattice Parameter for the III-V family of semiconductors at 300 K. The coordinates for Si and Ge are also included.

designed, lattice matched tandem cells the number of III-V materials choices appear limited.

Thus, an important problem to consider for tandem cells is the effect of lattice mismatch on photovoltaic performance. By relaxing the previously mentioned lattice matching constraint, several new alloy combinations with optimum bandgap values become available for monolithic tandem cells. In the case of mechanically stacked tandem cells, a similar situation exists due to the limited number of commercially available single-crystal substrates for epitaxial growth, since, in general, the individual subcells to be stacked would first be fabricated on lattice mismatched substrates. Therefore, it is clear that an effective utilization of lattice mismatched material configurations would be advantageous for tandem solar cells.

It is well known that lattice mismatched heterostructures contain crystalline defects, primarily in the form of misfit and threading dislocations, which serve to relieve the strain between the dissimilar crystal lattices. Such defects act as excess minority carrier recombination centers and enhance current leakage in p-n junctions. It is not clear, however, the degree to which such defects affect photovoltaic performance since controlled experimental studies in this area have not been performed. Furthermore, modeling studies on this subject have been few and are difficult to evaluate due to the lack of experimental data. It has been suggested, for example, that threading dislocation densities as high as 10^9 cm^{-2} might be acceptable for solar cell heterostructures with buried lattice mismatch, especially for devices operated under concentrated sunlight [3]. Recent calculations, however, indicate that dislocation densities lower than $5x10^5$ cm^{-2} are necessary in order to obtain high conversion efficiencies for thin-film GaAs solar cells grown on Si substrates [4]. Clearly, the discrepancies between different theoretical predictions need to be resolved *via* an expansion of the experimental data base. Therefore, in order to exploit fully the potential of III-V materials for tandem cell applications, it is important that the effects of lattice mismatch on pho-

tovoltaic performance be carefully studied experimentally.

1.2 Project Concept, Scope and Objectives

The $GaAs_{1-x}P_x$/GaAs system was chosen for this study for several important reasons. Firstly, $GaAs_{1-x}P_x$ is one of the leading candidates as a high-bandgap material for tandem cell applications since it offers direct bandgaps in the optimum range for top cells and has a broad technology base due to its application to visible light emitting diodes (LED's). Secondly, $GaAs_{1-x}P_x$ is lattice mismatched to GaAs and, therefore, provides a convenient means of studying the lattice mismatch problem. Thirdly, high-quality, single-crystal epilayers of $GaAs_{1-x}P_x$ can be grown on GaAs substrates by atmospheric pressure metalorganic vapor phase epitaxy (APMOVPE). Finally, the crystalline defects occurring in $GaAs_{1-x}P_x$ heterostructures have been characterized extensively in previous investigations thus providing useful background information for the present study.

A method for studying the lattice mismatch problem in a systematic manner was devised using the $GaAs_{1-x}P_x$/GaAs heterostructure illustrated in Figure 1.3. The structure consists of three major components including, from bottom to top, a p^+-GaAs substrate, a region of compositionally graded p^+-$GaAs_{1-x}P_x$ of variable thickness and an n^+/p $GaAs_{0.74}P_{0.26}$ shallow homojunction (SHJ) with a nominal junction depth of 50 nm and a base layer thickness of 5 μm. An extremely shallow junction is utilized in order to keep the fraction of incident light absorbed in the emitter layer as small as possible and thereby reduce photocurrent losses due to surface recombination.

The $GaAs_{1-x}P_x$ layers in the structure are formed using an epitaxial crystal growth process (APMOVPE) described in later sections. The GaAs substrate and $GaAs_{1-x}P_x$ graded region

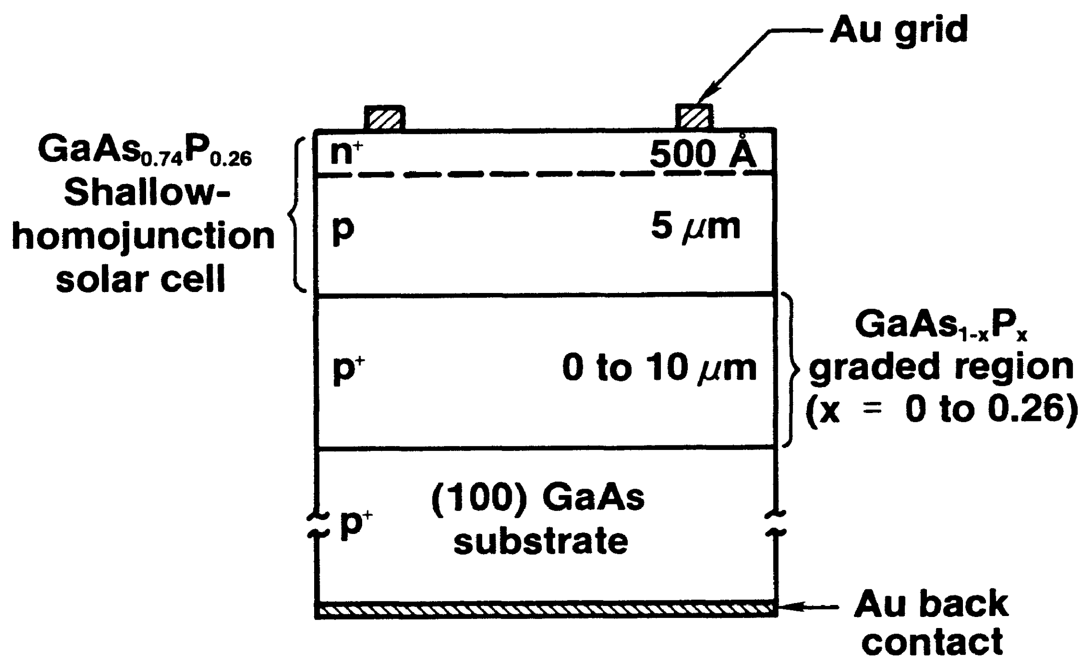

Figure 1.3 A schematic cross section of the compositionally graded $GaAs_{1-x}P_x/GaAs$ heterostructure used to produce $GaAs_{0.74}P_{0.26}$ shallow homojunctions with varying defect densities.

are both heavily doped p-type (5 - $10x10^{19}$ cm^{-3}) to ensure high electrical conductivity through the bulk of the structure. The doping levels in the n^+- and p-layers of the SHJ are $5x10^{18}$ cm^{-3} and $1x10^{17}$ cm^{-3}, respectively. Ohmic, low-resistance electrical contacts are formed on the front and back surfaces of the structure using pure gold, with the back contact covering the entire back surface and the front contact being in the form of a low-coverage grid in order to admit light to the junction. The composition of the graded region is varied from x = 0 to x = 0.26 using either uniform, discrete steps in x or by continuously varying x in a linear fashion. As shown later, the lattice mismatch between $GaAs_{1-x}P_x$ and GaAs increases linearly with x which implies that the compositional gradient and the strain gradient within the graded region are proportional to one another. The composition of the SHJ layers is held constant at a nominal value of x = 0.26 in order to keep the bandgap constant at 1.74 eV (i.e., a near-optimum value for a top cell in a two-junction tandem operated under one-sun terrestrial illumination, 25°C). The values of the layer thicknesses and doping levels used for the $GaAs_{0.74}P_{0.26}$ SHJ are identical to those used in fabricating high-efficiency GaAs SHJ cells in previous work [5], however, they are not necessarily optimum for $GaAs_{0.74}P_{0.26}$. The doping concentrations were determined from calibrations based on Hall Effect measurements made on single-layer samples grown previously. In addition, it was possible to use C-V techniques to confirm the the doping levels in the p-type base layers of the actual samples used in this work since the junctions are one-sided.

Preliminary experiments with the $GaAs_{1-x}P_x$/GaAs compositionally graded heterostructure showed that the dislocation type, density and morphology in the $GaAs_{0.74}P_{0.26}$ SHJ could be varied substantially by adjusting the parameters characterizing the graded region. This observation formed the basis for the present study since it implied that nominally identical $GaAs_{0.74}P_{0.26}$ SHJ's with different defect densities and morphologies could be prepared, characterized and compared by varying the design parameters of the compositionally graded

region. Additionally, using this approach the characteristics and effectiveness of different grading schemes can also be evaluated. Thus, even though the lattice mismatch between the $GaAs_{0.74}P_{0.26}$ SHJ and the GaAs substrate is constant, the effects of the mismatch can be varied and studied carefully by systematically varying the graded region design.

As mentioned above, the composition in the graded region can be varied in discrete steps or continuously. The parameters which characterize step-graded structures are the number of compositional steps and the total thickness of the graded region between the GaAs substrate and the base of the $GaAs_{0.74}P_{0.26}$ SHJ p-layer. For a step grade with uniform compositional steps, the magnitude of the compositional increment at a step is given by

$$\Delta x_{st} = \frac{x_{sc}}{n} \quad 1.1$$

and the thickness of each layer in such a graded region is given by

$$\Delta t_{st} = \frac{t_{GL}}{(n-1)} \quad 1.2$$

since the last compositional step occurs at the base of the p-layer in the SHJ. In the case of a continuous, linear grade, the defining parameter is the P concentration gradient within the graded region given by

$$G = \frac{x_{sc}}{t_{GL}} \quad 1.3$$

Nine different compositional grades were considered in this study including seven different step grades, a continuous, linear grade and no grade at all (i.e., the $GaAs_{0.74}P_{0.26}$ SHJ was grown directly on the GaAs substrate). Details of these are described in subsection 4.1.

In all cases, the n+/p SHJ device structures in the top layers of constant composition were identical so that the photovoltaic characteristics of the solar cells fabricated therein would be influenced only by the different defect densities, defect morphologies and other effects related to the lattice mismatch and graded region design. For high-efficiency solar cells, excessively thick epitaxial structures are difficult to justify since cell fabrication costs need to be reduced as far as possible. Therefore, an arbitrary upper limit of 10 μm was chosen for the graded layer thickness. The majority of the effort in this study has been devoted to step grades since previous studies have shown these to be more effective than continuous grades for thin graded regions.

A study of this type embraces a wide range of technical disciplines and, therefore, a detailed description and analysis of every facet of the work could be very lengthy. For example, the sections of this thesis dealing with defect analysis and device analysis might be considered alone as being appropriate thesis topics if discussed in full detail. With this in mind, it is important that the scope and objectives of the present work be clearly defined. The scope is limited to an empirical determination of the overall effects of lattice mismatch on the photovoltaic performance of $GaAs_{0.74}P_{0.26}$ SHJ solar cells. The effects of lattice mismatch can be considered in two parts; those due to the defects formed by the mismatch, and those due to the variations in the design of the graded region, both of which are necessarily related. With these ideas in mind, the primary objectives of this work are outlined as follows:

1. To evaluate the effects of dislocations on the photovoltaic characteristics.

2. To investigate the effectiveness and characteristics of thin (i.e., <10 μm) compositional grades of both types (i.e., stepped or continuous).

3. To identify the parameters associated with thin lattice mismatched heterostructures that most critically affect photovoltaic performance.

The remaining sections outline the technical background, experimental procedures and experimental results and conclusions. The technical background provided in Section 2.0 includes a discussion of the properties of $GaAs_{1-x}P_x$ and defects observed in $GaAs_{1-x}P_x$/GaAs heterostructures. The photovoltaic device performance parameters are also discussed in this section along with the anticipated effects of defects on device performance. Section 3.0 describes the experimental procedures which includes a description of the epitaxial growth of the $GaAs_{1-x}P_x$/GaAs structures, fabrication of the $GaAs_{0.74}P_{0.26}$ SHJ solar cells and material/device characterization techniques which were used. A discussion of the experimental results is given in Section 4.0 which leads to the conclusions and suggestions for future work in this area which are summarized in Section 5.0.

2.0 TECHNICAL BACKGROUND

2.1 Introduction

This section provides some of the necessary technical background for the discussion of experimental results given in Section 4.0. Subsection 2.2 covers some of the fundamental structural and optoelectronic properties of $GaAs_{1-x}P_x$ relevant to both the lattice mismatch problem and the design and operation of $GaAs_{0.74}P_{0.26}$ SHJ solar cells. The defects observed in $GaAs_{1-x}P_x$/GaAs heterostructures are also described in this subsection. Parameters which define solar cell performance are introduced in Subsection 2.3 along with a discussion of the anticipated effects of defects on these parameters.

2.2 $GaAs_{1-x}P_x$/GaAs Epitaxial Heterostructures

2.2.1 Properties of $GaAs_{1-x}P_x$

Like most III-V semiconductor compounds, $GaAs_{1-x}P_x$ crystallizes in a tetrahedrally coordinated zincblende lattice with the bonding between the Group III and Group V atoms being primarilary covalent. It is often referred to as being a pseudobinary alloy of the binary III-V compounds GaAs and GaP. The $GaAs_{1-x}P_x$ zincblende structure consists of two interpenetrating face-centered cubic (FCC) lattices, one containing the Ga atoms and the other the As and P atoms (i.e., the Group III and Group V sublattices). The body diagonal of either FCC lattice defines the [111] direction and the two face-centered cubes are displaced from each other by 1/4 of a body diagonal along that direction. The lattice parameter for a zincblende compound of this type is given by the length of the FCC lattice cube side. For $GaAs_{1-x}P_x$, the lattice parameter is determined by assuming the validity of Vegard's Law (i.e.,

that the ternary lattice parameter is given by a linearly weighted average of the binary constituent lattice parameter values) and using the lattice parameters for GaAs (5.653 Å) and GaP (5.451 Å) at 300 K. Thus, the lattice parameter as a function of the P mole fraction is written as

$$a(GaAs_{1-x}P_x, 300K) = [5.653 - (0.202)x]\text{Å} \qquad 2.1$$

From this expression, the lattice mismatch for $GaAs_{1-x}P_x$ grown epitaxially on a GaAs substrate can be calculated and is given by

$$\frac{\Delta a_{e-s}}{a_s}(x, 300K) = \frac{(a_e - a_s)}{a_s} = -(3.57 \times 10^{-2})x \qquad 2.2$$

$$(0 \leq x \leq 1)$$

where the minus sign indicates that the epitaxial layer is in biaxial tension. Therefore, for x = 0.26 the lattice mismatch is -0.93%.

The key optoelectronic parameters relevant to the operation of photovoltaic devices include the semiconductor energy gap and the optical absorption coefficient. The bandgap at 300 K for GaAs is direct with a value of E_g = 1.43 eV while for GaP it is indirect with E_g = 2.26 eV. This results in $GaAs_{1-x}P_x$ exhibiting a bandgap which has a direct-to-indirect transition at x_c = 0.49. The bandgaps of interest for tandem cell applications fall within the direct bandgap composition range (i.e., for x = 0 - 0.49). Due to atomic disorder on the Group V sublattice, the direct bandgap portion of the composition range varies slightly sublinearly with x [6]. The sublinearity is described using an empirically derived optical bowing parameter which gives a best fit to experimental data using a parabolic form for E_g (x). For III-V materials, it is found that optical bowing corrections tend to increase as the mean

bandgap of the binary constituents of the alloy decreases. For the $GaAs_{1-x}P_x$ system, the sublinear correction is small, however, it is worth accounting for and $E_g(x)$ is written as follows [7]

$$E_g(x,300K) = \left[0.210x^2 + 1.091x + 1.441\right]eV \qquad 2.3$$

$$(0 \leq x \leq 0.49)$$

A plot of this function is given in Figure 2.1 showing E_g *vs* x and also indicating the $GaAs_{1-x}P_x$ device composition (x = 0.26) and bandgap (E_g = 1.74 eV) used in this study.

Optical absorption in a semiconductor is defined in terms of an absorption coefficient which is a function of the wavelength of light impinging on the semiconductor surface. The variation of photon flux with depth is given by Beer's Law as

$$\Gamma(d,\lambda) = \Gamma_0(\lambda)\exp\left[-\alpha(\lambda)d\right] \qquad 2.4$$

Using this expression, the minimum solar cell layer thickness required for complete optical absorption can be calculated. Unfortunately, detailed data regarding the absorption coefficient for $GaAs_{1-x}P_x$ are apparently unavailable. However, since $GaAs_{0.74}P_{0.26}$ is GaAs-rich and has a direct bandgap it is reasonable to assume that the near-bandedge absorption coefficients for $GaAs_{0.74}P_{0.26}$ and GaAs are approximately equal. Using a value of $\alpha = 10^4$ cm^{-1}, a good estimate of the minimum required thickness can be made. For the p-layer thickness used in the $GaAs_{0.74}P_{0.26}$ SHJ (5 μm), a calculation of the photon flux at the back edge of the p-layer with respect to the incident photon flux yields

$$\frac{\Gamma(d = 5\mu m)}{\Gamma_0} = \exp(-5) \cong 0.7\% \qquad 2.5$$

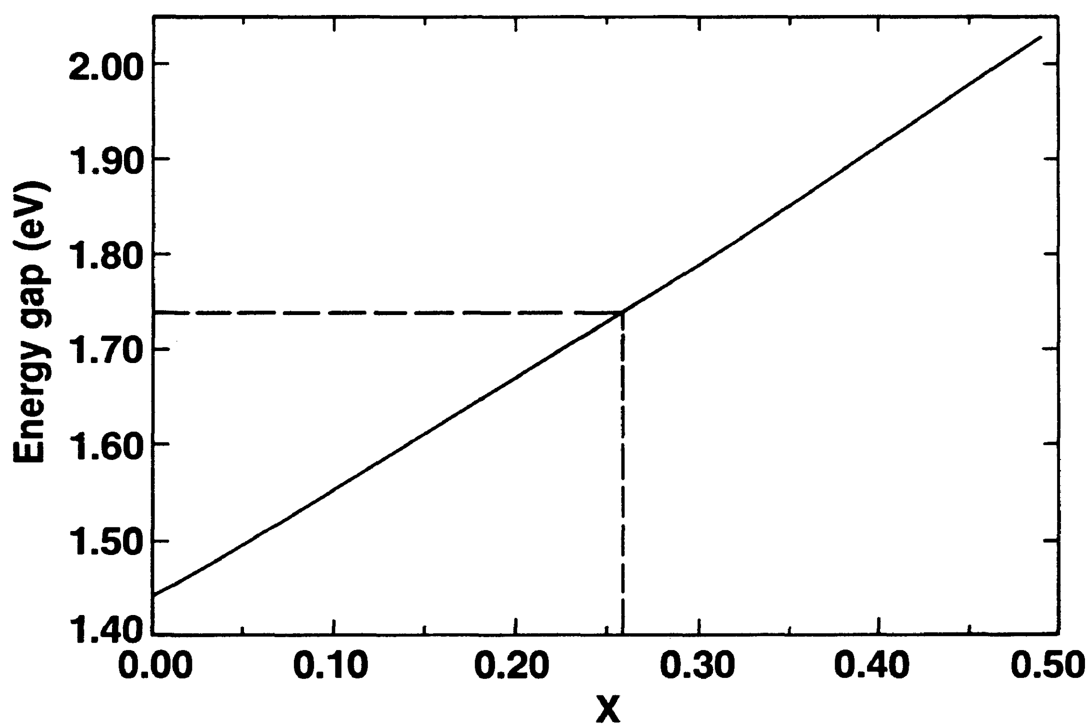

Figure 2.1 Energy Gap *vs* x for $GaAs_{1-x}P_x$ at 300 K. The dotted lines indicate the average composition (x = 0.26) and energy gap (E_g = 1.74 eV) for the devices used in this study.

Thus, it is expected that nearly all photons with energies greater than or equal to 1.74 eV will be absorbed well within the $GaAs_{0.74}P_{0.26}$ SHJ cell layers. These calculations indicate that the SHJ cell design chosen for this study is adequate for efficient operation and should therefore provide meaningful data as to the effects of defects in the cell layers.

2.2.2 Defects in $GaAs_{1-x}P_x$/GaAs Heterostructures

The defects in $GaAs_{1-x}P_x$/GaAs heterostructures arising from lattice mismatch were studied extensively in the late 1960's to early 1970's due to the interest in developing highly efficient visible LED's. In these studies, the samples were prepared using chloride-transport Vapor Phase Epitaxy (VPE) and thick (20-60 μm) compositionally graded regions using a linear phosphorus gradient were employed. By the middle 1970's, the spectrum of lattice mismatched III-V materials under investigation had expanded considerably and techniques designed to reduce defect densities in device layers were being developed and explored. More recently, $GaAs_{1-x}P_x$/GaAs heterostructures grown by MOVPE, including strained-layer superlattices and solar cells, have been studied.

Abrahams *et al.* [8] have extensively studied dislocations in $GaAs_{1-x}P_x$ graded layers grown by VPE on GaAs substrates using transmission electron microscopy (TEM) and have shown that there are two general types of dislocations present. The first type is a misfit dislocation which forms networks in the compositionally graded layer and serves to accomodate the lattice mismatch due to the variation of the lattice parameter with the change in composition. The second type is the so-called inclined or threading dislocation which arises out of the misfit dislocation network and propagates along with the growing epilayer into the final layer of constant composition where a device is typically formed. Abrahams argued that inclined dislocations occur because misfit dislocations, which in a perfect crystal

would extend from one edge of the specimen to the other, are segmented due to variations in the epitaxial growth process and , therefore, must bend upwards into the plane of growth. Based on this concept, Abrahams developed a model to predict the threading dislocation density as a function of the length of misfit dislocation segments. It was also noted that in continuously graded samples the threading dislocation density decreased as the compositional gradient was decreased. Misfit dislocations in $GaAs_{1-x}P_x$ lie along [110] directions and therefore lie in the plane of growth when (100)-oriented substrates are used, thus implying that inclined dislocations must necessarily intersect the growth plane. Abrahams also investigated dislocation interactions and lattice-mismatch-induced stresses in $GaAs_{1-x}P_x$/GaAs structures.

In a related theoretical study, Saul [9] demonstrated the importance of the compositionally graded region in such heterostructures in reducing the detrimental effects of both lattice mismatch and stresses attributable to thermal expansion differences during growth. Kishino *et al.* [10] observed that the cross-hatch pattern which generally forms on the surface of lattice mismatched epilayers was indicative of an underlying misfit dislocation network. Mader *et al.* [11] investigated the details of dislocation morphology in $GaAs_{1-x}P_x$/GaAs graded samples and derived a value for the stacking fault energy in $GaAs_{0.7}P_{0.3}$ through a TEM analysis of extended dislocations.

Olsen *et al.* [12] described an improved compositional grading technique for mismatched III-V heterostructures which involved the use of abrupt compositional steps in the grading process (i.e., a step grade). Such a procedure was described as having several advantages since lower threading dislocation densities were achieved using thinner compositionally graded regions. However, it was noted that the procedure did not always work well for epilayers in biaxial tension since cracking of the grown film was often observed to occur. The

technique worked very well for epilayers in biaxial compression. The lower threading dislocation densities achieved with this technique were attributed to the fact that a large fraction of the threading dislocations originating from a misfit dislocation network at a previous compositional step bend over into the misfit configuration upon encountering a subsequent step.

Review articles describing the effects of lattice mismatch in III-V compounds have been provided by Olsen [13] and Schiller *et al.* [14]. In these, the microstructural and macrostructural effects of the mismatch in $GaAs_{1-x}P_x$/GaAs structures are discussed. Olsen noted that the severity and morphology of surface cross hatching depends upon the amount of lattice mismatch and whether the epilayer is in biaxial tension or compression; epilayers in tension tend to have rougher surfaces. Further reductions in the threading dislocation density through the use of strained-layer superlattices have been reported by some authors [15], however, such structures are often not easily prepared [16] and have proven to be unstable under certain conditions [17]. Recently, high-performance solar cells have been fabricated in $GaAs_{1-x}P_x$ epilayers using step graded structures [18, 19].

2.3 Photovoltaic Device Performance Theory

2.3.1 Device Performance Parameters

The theory of n/p homojunction solar cells is well established and has been presented by a number of authors [20, 21, 22]. For an n/p diode in the dark, the J-V characteristic is calculated by solving the minority carrier continuity and current equations subject to boundary conditions governing the concentration of excess minority carriers at both edges of the depletion region and at the front and back surfaces of the diode. It is assumed in the

calculation that the diode is ideal in the sense that parasitic resistive losses do not occur. Such a procedure results in an expression for the injected current as a function of applied voltage of the following form

$$J = J_0\left[\exp\left(\frac{qV}{kT}\right) - 1\right] \qquad 2.6$$

The reverse-saturation current density J_0 generally depends on a number of factors including the intrinsic carrier concentration, extrinsic impurity doping levels, diode geometry, minority carrier diffusivity and diffusion length and the recombination velocities at the front and back surfaces of the diode. Furthermore, if recombination/generation of minority carriers occurs in the diode depletion region through mid-bandgap states, the form for J_0 must be adjusted to include this additional current component. Practically, a single-exponential form is preferred and a modified form of equation 2.6 given by

$$J = J_{00}\left[\exp\left(\frac{qV}{FkT}\right) - 1\right] \qquad 2.7$$

yields a very close approximation to the actual J-V characteristic. In this expression, the junction ideality factor F and the preexponential factor J_{00} are used to approximate the injected and recombination/generation current density components by a single term. This approximation greatly simplifies the form for the illuminated J-V characteristic for a solar cell. F and J_{00} are usually determined by plotting actual forward-bias *ln*J *vs*V data. F is derived from the slope of such a plot and J_{00} is given by the intercept with the *ln*J axis. At low forward voltages, recombination/generation currents constitute the majority of J_{00} resulting in F having a value of 2. For high forward bias, injected minority carrier currents dominate J_{00} giving F = 1.

The photocurrent J_L generated by a solar cell is determined by the absolute external quantum efficiency (AEQE) of the cell and the characteristics of the incident solar spectrum according to the following expression

$$J_L = q\int_0^\infty AEQE(\lambda)\frac{d\Gamma(\lambda)}{d\lambda}d\lambda \qquad 2.8$$

which is simply the integral of the product of the monochromatic AEQE and the solar photon flux per unit wavelength, over all wavelengths. With complete knowledge of the parameters which characterize the cell properties (i.e., material properties, dimensions and minority carrier transport properties), the AEQE can be calculated. Alternatively, the AEQE can be measured in the laboratory. Under ideal conditions, the principle of superposition of the component current densities is valid and the J-V characteristic for a solar cell under illumination is written

$$J = J_{00}\left[\exp\left(\frac{qV}{FkT}\right) - 1\right] - J_L \qquad 2.9$$

Typical dark and illuminated J-V characteristics for an ideal solar cell are illustrated in Figure 2.2. When the cell is illuminated, it is desirable to operate at the maximum power point on the J-V characteristic as shown in the diagram.

The performance of a solar cell is usually rated according to its energy conversion efficiency which is simply the ratio between the electrical power output and the incident photonic power. Practically, the efficiency is expressed in terms of three parameters (V_{oc}, J_{sc} and FF) which can each be derived from the illuminated J-V characteristic for a cell. Accordingly, the efficiency can be written as follows

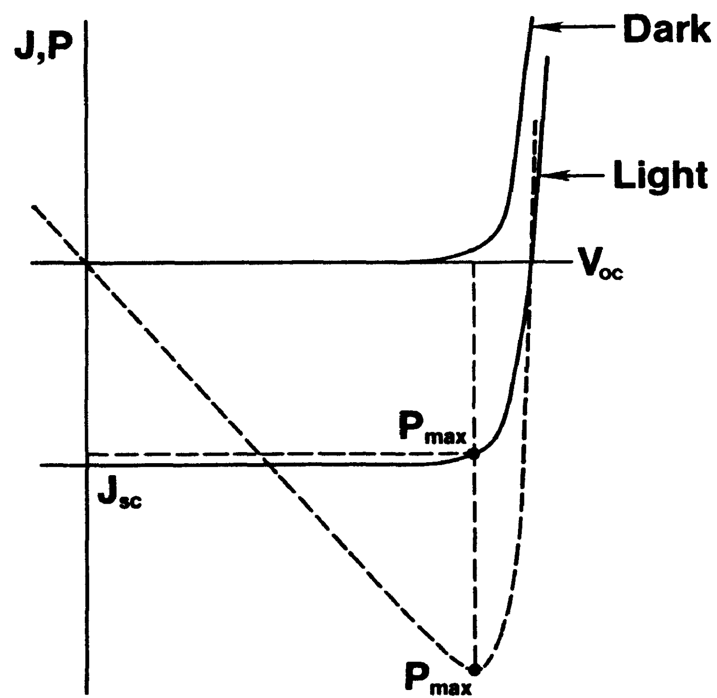

Figure 2.2 Illuminated and dark J-V characteristics for an ideal solar cell. The power output is given by the dashed curve.

$$\eta = \frac{V_{oc} J_{sc} FF}{P_i} \tag{2.10}$$

where P_i is the incident areal solar power density. V_{oc} is determined by setting J = 0 in equation 2.9 which gives

$$V_{oc} = \frac{FkT}{q} \ln\left(\frac{J_L}{J_{00}} + 1 \right) \tag{2.11}$$

Thus, V_{oc} for a particular cell is governed by its dependence on J_{00} and J_L. J_{sc} is obtained with equation 2.9 for V = 0, yielding the simple result

$$J_{sc} = -J_L \tag{2.12}$$

Therefore, J_{sc} is limited by factors which affect the AEQE such as the minority carrier diffusion length and the cell reflectance. Finally, FF is defined by the following expression

$$FF = \frac{P_m}{V_{oc} J_{sc}} = \frac{V_m J_m}{V_{oc} J_{sc}} \tag{2.13}$$

where P_m is the maximum power density deliverable by the cell and J_m, V_m are the coordinates of the maximum power point on the illuminated J-V characteristic. Ideally, FF is a function of V_{oc} only and can be expressed as such to a very close approximation with the following formula

$$FF = \frac{v_{oc} - \ln(v_{oc} + 0.72)}{v_{oc} + 1} \tag{2.14}$$

where

$$v_{oc} = V_{oc}\left(\frac{kT}{q}\right)^{-1} \qquad 2.15$$

This formula is valid for $v_{oc} > 10$ (i.e., for most photovoltaic materials). Each of the solar cell parameters defined above for an ideal cell can be measured easily in the laboratory for an actual cell.

2.3.2 Anticipated Effects of Defects On Device Performance

As described previously, two general types of dislocations (misfit and threading) are present in compositionally graded $GaAs_{1-x}P_x$ heterostructures. It is anticipated that the manner in which each type affects cell performance will depend upon their respective density and configuration in the cell layers. Previous studies of GaAs LED's and GaAsSb photodiodes demonstrate that dislocations degrade the emission efficiency and quantum efficiency, respectively, of such devices [23, 24]. Hence, dislocations are expected to have a similar effect on the quantum efficiency, and therefore the J_{sc}, of $GaAs_{0.74}P_{0.26}$ solar cells. Furthermore, recent results for GaAs solar cells grown on Si substrates [25] show that dislocations can significantly degrade V_{oc} thus suggesting that similar effects should prevail in $GaAs_{0.74}P_{0.26}$ cells.

A solar cell is a thin, large-area, planar device. Misfit dislocations lie parallel to the growth plane and can therefore occupy large lateral regions of the cell layers. On the other hand, threading dislocations, on average, lie nearly parallel to the growth direction and thus occupy small volumes in the cell layers. Moreover, due to their configuration threading dislocations must intersect the cell junction. These observations lead to some important implications: i) Overall, misfit dislocations should prove to be far more harmful to cell performance than threading dislocations due to the larger cell layer volume occupied by a

single misfit dislocation. ii) It should be possible to minimize the deleterious effects of misfit dislocations by confining misfit dislocation networks to regions well below the cell layers. iii) It is impossible to keep threading dislocations from passing through the cell junction, therefore, threading dislocations will necessarily affect the junction characteristics.

In considering the effects of defects on the cell performance parameters, it is necessary to consider only J_{sc} and V_{oc} due to the dependence of FF on V_{oc}. It is clear that both types of dislocations will degrade J_{sc} since they behave as minority carrier recombination sinks, with misfit dislocations being more effective in this regard for the reasons explained above. V_{oc} will also suffer from the presence of defects in the vicinity of the cell junction since dislocations are known to act as shunt paths through n/p junctions. Due to the complexity of the various defect configurations which might arise in the junction region, it is very difficult to provide an all-encompassing model of the influence of dislocations on the cell junction characteristics. Nevertheless, for the purpose of illustration it is useful to model the dislocation shunting effect using the equivalent circuit shown in Figure 2.3(a). In this circuit, a shunt resistor R_{sh} is placed in parallel with the solar cell which is shown as a parallel combination of a diode and a photocurrent generator. The shunt resistor is intended to approximate the shunting effects of dislocations in the cell junction. Using superposition, it is possible by graphical construction to visualize the effects of the shunt resistor on the solar cell I-V characteristic, as shown in Figure 2.3(b). I_{sc} is not affected, however V_{oc} and FF are both reduced by the presence of the shunt.

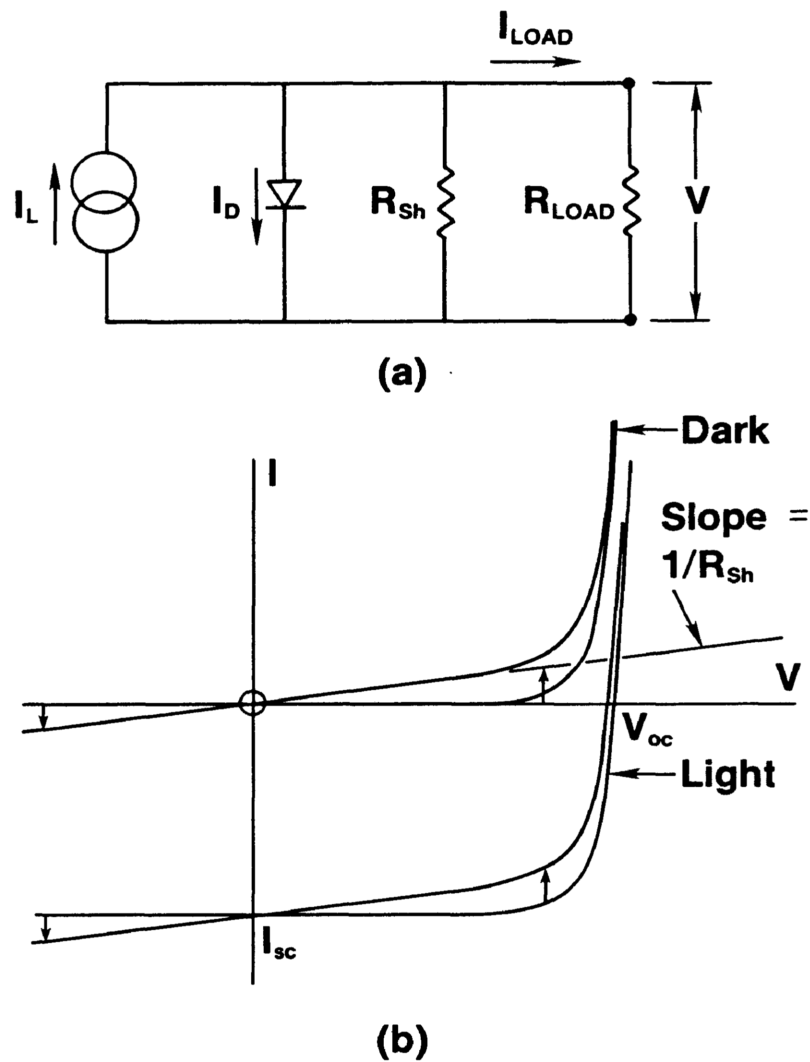

Figure 2.3 (a) Simplified equivalent circuit for a solar cell with finite shunt resistance R_{sh}. (b) The effect of shunt resistance on the I-V characteristic of an ideal solar cell by graphical construction.

3.0 EXPERIMENTAL PROCEDURE

3.1 Introduction

The experimental procedures involved in the epitaxial growth, fabrication and characterization of the $GaAs_{0.74}P_{0.26}$ SHJ cells are discussed in this section. Emphasis is placed on the epitaxial growth procedures since they played the most critical role in the success of this project. A general description of the APMOVPE process is included which is followed by a detailed discussion of the SERI home-built APMOVPE system and the growth conditions and techniques used. $GaAs_{0.74}P_{0.26}$ SHJ solar cell processing steps and material/device evaluation techniques are also outlined.

3.2 Growth of $GaAs_{1-x}P_x$/GaAs Heterostructures by APMOVPE

3.2.1 General Description of APMOVPE

Through the last decade, MOVPE has rapidly developed to become the technique of choice for producing device-quality, thin-film III-V compound semiconductor heterostructures. Several recent reviews of MOVPE growth technology have been published which outline the growth chemistry, system design considerations, quality and uniformity of epitaxial materials, device applications and results and other aspects [26 - 30]. Due to its inherent simplicity, controllability and scalability, MOVPE is considered to be the most logical candidate for future large-scale applications of III-V epitaxial materials.

With MOVPE, epitaxial growth is achieved *via* the pyrolysis/catalysis of an appropriate mixture of metalorganic (MO) and hydride source vapors diluted in a suitable carrier gas

stream which is passed over a hot, single-crystal substrate. Using such sources, the overall chemical reaction most commonly used for the growth of III-V compounds is given in general form as

$$R_mM + XH_m \rightarrow MX + mRH \qquad 3.1$$

Typically, M is a group III element, X is a group V element and R is an organic radical. Equation 3.1 represents the net chemical reaction, however, the intermediate reactions, including homogeneous decomposition of precursors in the gas phase and heterogeneous surface reactions on the substrate, can be quite complex and are not completely understood. For III-V compounds of the type (III)$As_{1-x}P_x$, a high groupV-to-group III ratio must be maintained during growth (typically 10 and often much higher) since both As and P in the solid phase are highly volatile at the required growth temperatures. Accordingly, under these conditions the epilayer growth rate is proportional to the arrival rate of the Group III species to the substrate surface. Intentional doping (n- or p-type) of the growing film is achieved by introducing suitable amounts of gaseous molecular species containing elements from, for example, groups VI or II, respectively. This type of reaction applies to the growth of $GaAs_{1-x}P_x$ epilayers on GaAs substrates as performed in this study and discussed in the next subsection. The net chemical reaction for the growth of $GaAs_{1-x}P_x$ using $(CH_3)_3Ga$, AsH_3 and PH_3 as reactants under the conditions used in this study is written as follows

$$(CH_3)_3Ga + k(AsH_3) + l(PH_3) \xrightarrow{H_2, 750°C} GaAs_{1-x}P_x + 3CH_4 \qquad 3.2$$

As discussed in sub-subsection 4.2.2, with this combination of reactants the P mole fraction (x) obtained in the growing film varies sublinearly with the mole fraction of P in the vapor phase. The relationship between k, l and x is defined in terms of a vapor/solid P distribution

coefficient (K_p) which is also described in sub-subsection 4.2.2.

The growth reaction takes place in a reactor vessel which is usually constructed of fused quartz, thereby providing a reactor which is transparent, chemically inert, easily cleaned and which has a melting point substantially higher than typical growth temperatures (500-800°C). The reactor walls can be cooled by natural air convection or through the use of an outer jacket with a flowing coolant such as water. Growth may take place under atmospheric or reduced pressures. Under atmospheric pressure conditions, the growth process is diffusion-limited due to the presence of a stagnant boundary layer above the substrate surface through which reactants must diffuse in order to reach the growing crystal surface. High growth temperatures are necessary in order to provide sufficient thermal energy to crack the MO and hydride molecular nutrient species as well as to enhance the mobility of adsorbed species on the substrate surface which results in higher epilayer quality and improved surface morphlogy. The pyrolytic/catalytic nature of the process requires that only the substrate be heated to assure efficient deposition, thus simplifying the temperature control involved during growth. This is usually achieved by placing the substrate on a graphite susceptor residing in the reactor vessel which is heated using either radio-frequency (RF) induction, quartz-halogen lamps or electric heating elements and the temperature is controlled using commercially available feedback-type controllers in conjunction with a thermocouple or optical pyrometer to monitor the temperature.

Reactor vessels are usually cylindrical in cross section with their axes oriented either vertically or horizontally and either type has associated advantages and disadvantages. Reactor geometry is the parameter most critical to the resulting properties of grown layers since thickness profiles, growth chemistry and parasitic phenomena are all strongly affected by the hydrodynamic and thermal effects induced by a particular reactor configuration.

Computer modeling studies of the effects of reactor geometry have been the subject of intense study in recent years and useful guidelines for designing reactors have resulted. However, in many cases the reactor design is empirically optimized for a particular application due to the complexities involved with practical reactors. Through proper design of the reactor geometry and choice of growth conditions, both of which influence the characteristics of the stagnant boundary layer and the growth chemistry, it is possible to achieve highly uniform deposition. Choice of reactor vessel design can depend on a wide variety of factors including the types of materials and heterostructures which will be grown and the degree of growth uniformity and heterointerface abruptness that is required. For device applications, demanding requirements are placed on reactor performance since tight control over epilayer morphology, uniformity and heterointerface abruptness is a critical prerequisite to the realization of devices with near-theoretical characteristics. Additional features which are desirable in a reactor vessel include efficient utilization of reactants, ease of fabrication, substrate loading and maintainence and minimization of the number of component parts and external connections which must be made. Such factors play important roles in operating the growth system in a safe, economical and consistent manner.

The MOVPE process is highly controllable since it is based on well-developed gas handling and precursor synthesis technologies. Epilayer purity is determined by the amount and type of residual impurities in the source materials, internal cleanliness of the gas handling hardware and external atmospheric leakage into the growth system. Source purity has improved steadily during recent years and is now at an advanced stage of development for the more commonly used precursors. Through the use of internally electropolished stainless steel tubing and high-integrity welded and/or metal-to-metal seal fittings and advanced elastomer seals, gas handling system contamination and leakage can be virtually eliminated. Such advancements have also had a positive effect on the safety aspects of the process.

Control of the epilayer growth process is achieved through precise regulation of the substrate temperature and the mass flow rates of the carrier gas and source vapors into the reactor. A carefully constructed gas handling system, typically consisting of a combination of pressure regulators, electronic mass flow controllers and pneumatically operated bellows or diaphragm valves connected together using seamless stainless steel tubing, is used for the purpose of controlling gas flow rates and switching source gases in and out of the reactor. A run/vent-style manifold is commonly used for switching and mixing the reactant vapors since it allows each source to flow continuously during a growth run and can be designed to eliminate pressure transients in the reactor. Using such components, automated computer control of the growth process is also possible thus offering the option of growing complex heterostructures incorporating features such as compositionally graded regions and ultra-thin multilayers.

Sources in high-pressure, gaseous form are easily metered using electronic mass flow controllers. However, MO sources, in either liquid or solid form, require a more complex metering system. As supplied by the vendor, MO sources are usually packaged in stainless steel cylinders with shutoff valves and a dip tube connected to the cylinder inlet. The reactant mass flow rate is controlled by passing a metered flow rate of a carrier gas through the cylinder, with the cylinder held at a constant temperature. By assuming that the carrier gas becomes fully saturated with the reactant vapor by the time that it exits the cylinder, it is possible to calculate the reactant mass flow rate leaving the cylinder. At the cylinder outlet, the flow rates are related to the partial pressures as follows

$$\frac{f_{MO}}{f_{H_2}} = \frac{P_{MO}}{P_{H_2}} \qquad 3.3$$

Using the law of partial pressures, at the cylinder outlet we have

$$P_0 = P_{MO} + P_{H_2} \tag{3.4}$$

Thus, the MO flow rate is related to the carrier gas flow rate according to

$$f_{MO} = \frac{P_{MO}}{P_0 - P_{MO}} f_{H_2} \tag{3.5}$$

MO source vapor pressure data as a function of temperature are available in the literature and from commercial vendors [31]. The most commonly used form for this relationship is given by

$$\log_{10} P_{MO}(mmHg) = B - \frac{A}{T} \tag{3.6}$$

where A and B are constants and T is in Kelvins.

Safe operation of MOVPE systems is a major concern due to the many hazards associated with the reactants which are employed. Besides high-quality gas-handling hardware, additional system features usually include separate heavy-guage steel gas cabinets for high-pressure source cylinders, ventilated enclosures for the gas-handling system and the reactor vessel, a reactor effluent scrubbing system and a toxic gas monitoring and alarm system. Additionally, automatic, fail-safe shutdown capabilities can be engineered into the system design as a means of dealing with emergency situations.

3.2.2 APMOVPE Apparatus and Source Materials

The APMOVPE system used to grow the $GaAs_{1-x}P_x$/GaAs structures for this study features a home-built gas-handling system coupled with a SERI-patented reactor vessel design [32]. A schematic illustration of the gas-handling system is given in Figure 3.1 showing the relationship between the sources and the major hardware components. The system is a run/vent type utilizing a split main mixing manifold composed of a series/parallel combination of air-operated 2-port (vent) and 3-port (run) bellows valve pairs which are each tied to a common high-pressure (80 psi.) air control line. Electric, 3-way solenoid valves are used to control the air pressure to the manifold valve pairs such that flipping a 2-pole electric toggle switch is all that is required to switch a source gas flow from vent to run and *vice versa*. The term "split" refers to a separation of the MO source vapors from the others until just prior to introduction into the reactor vessel. Such a manifolding arrangement allows for fast gas switching times and also reduces the possibility of homogeneous or heterogeneous reactions in the vapor phase preceding growth. Plumbing interconnections between each of the sources and the mixing manifold consist of 1/4" O.D (0.035" wall thickness), seamless 316 stainless steel tubing connected by a combination of leak-tight welded, VCR (metal gasket) and o-ring fittings with electronic mass flow controllers for metering the source gas flow rates. Manual bellows valves are also included at strategic points within the system for maintenance and leak checking purposes. Palladium-diffused hydrogen is used as the carrier gas throughout the system as well as for purging the source lines and reactor during idle periods. As shown, the $(CH_3)_3Ga$ and $(C_2H_5)_2Zn$ source cylinders are immersed in constant-temperature baths in order to keep the vapor pressure of each source constant. The characteristics of the various sources included in the system are summarized in Table 3.1. As defined in equation 3.5, the vapor pressure constants for $(CH_3)_3Ga$ and $(C_2H_5)_2Zn$ are A = 1703, B = 8.07 and A = 2190, B = 8.28, respectively. Due to the hazards associated with the source materials, the gaseous sources are housed in separate, ventilated gas cabinets and the entire gas-handling system is housed in a ventilated enclosure with sliding safety glass doors for ease of operation and

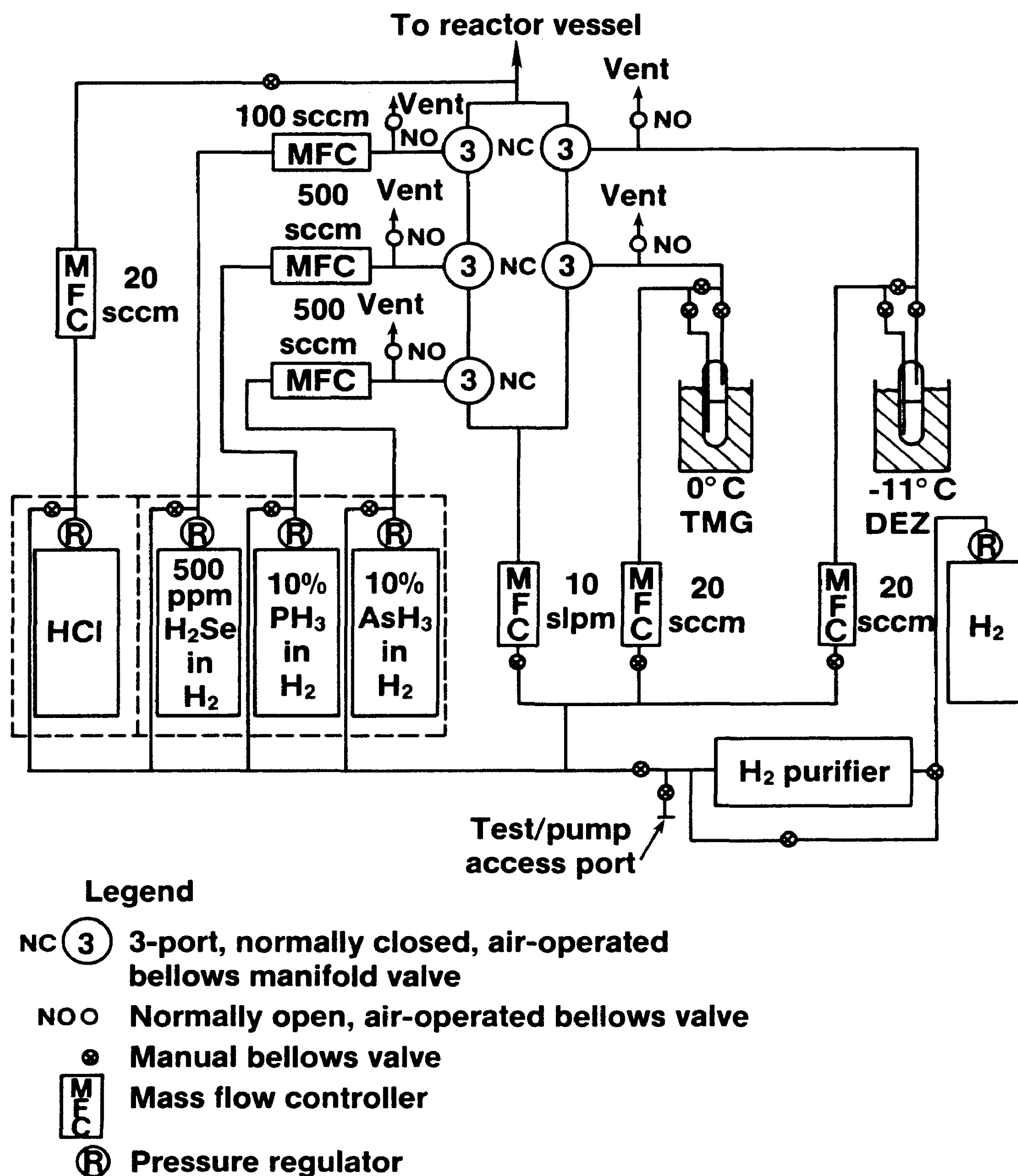

Figure 3.1 A schematic diagram of the APMOVPE gas handling system.

Table 3.1 Chemical reactants used in the APMOVPE process.

Reactant	Chemical Formula	Application	Vendor	Hazards
Trimethylgallium	$(CH_3)_3Ga$	Ga source	Alfa Products	Pyrophoric liquid
10% Arsine in Hydrogen	10% AsH_3/H_2	As source	Phoenix Research	Highly toxic, pyrophoric gas
10% Phosphine in Hydrogen	10% PH_3/H_2	P source	Phoenix Research	Highly toxic, pyrophoric gas
Diethylzinc	$(C_2H_5)_2Zn$	Zn source (p-doping)	Alfa Products	Pyrophoric liquid
500 ppm Hydrogen Selenide in Hydrogen	500 ppm H_2Se/H_2	Se source (n-doping)	Scientific Gas Products	Toxic, flammable gas
Hydrogen Chloride	HCl	Vapor etching susceptor	Scientific Gas Products	Highly corrosive, toxic gas
Hydrogen	H_2	System carrier/ purge gas	Linde	Flammable gas

maintenance. A centralized toxic gas monitoring system is used to check for source gas leaks and is in operation on a 24-hour-a-day basis at SERI.

Details of the reactor vessel are shown in the diagrams in Figure 3.2. As shown in Figure 3.2 (a), the reactor is a vertical, two-piece design with the main body constructed of a 50 mm O.D. fused quartz tube using a clamped o-ring seal to join the reactor top and bottom halves. Affixed to the reactor bottom half is the susceptor support rod which is open at the bottom end allowing a thermocouple to be inserted up into the interior of the susceptor for temperature measurement. Also included at the base of the reactor bottom is the exhaust port. The susceptor is cylindrical, 1.00" tall, 1.25" O.D. and is composed of high-purity graphite which is coated with a thin layer of silicon carbide in order to inhibit any out-gassing of trace impurities in the graphite. A small retaining lip is included around the outer edge of the susceptor to keep the substrate from sliding off during loading and unloading. Substrate heating is achieved using an RF generator with an induction coil located on the outside of the reactor top around a section which encloses the susceptor. Substrates are loaded into the reactor by breaking the o-ring seal, separating the reactor halves, placing the wafer on the top surface of the susceptor, re-joining the halves and re-sealing the reactor. Further details of the reactor dimensions are given in a recent United States patent [32].

The key feature in this reactor design with respect to reactor performance and epilayer quality is the gas inlet configuration. This special inlet design has resulted from an empirical study of different vertical reactor inlets and their effect on layer uniformity. Figures 3.2 (a), (b) and (c) show details of the gas inlet and the gas flow pattern in the vicinity of the susceptor. The inlet converts a single gas stream flowing vertically downward into two horizontal gas streams which enter the growth zone at diametrically opposed tangents with respect to the reactor walls. Thus, a downwardly spiralling vortex flow pattern is established. As a means

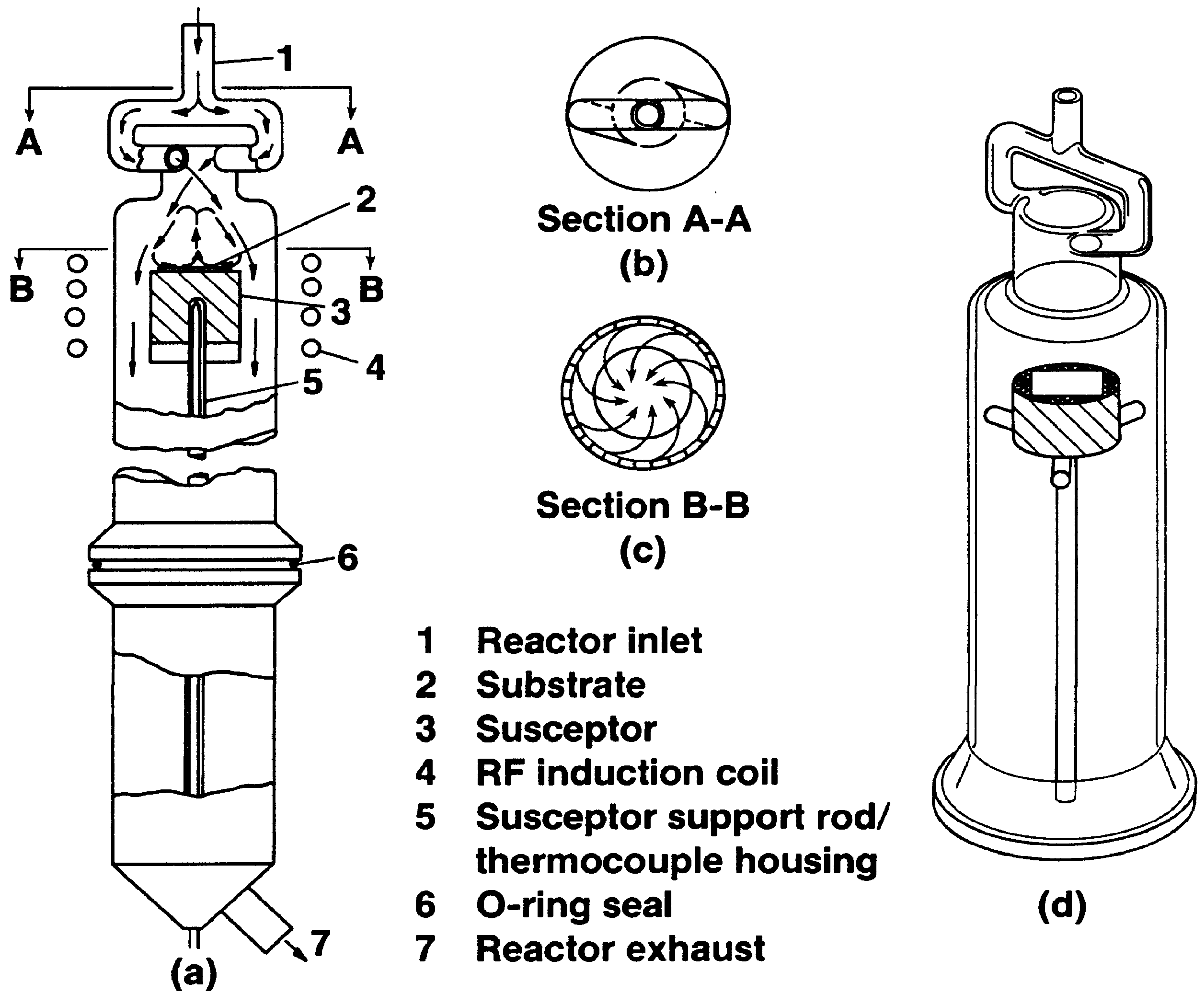

Figure 3.2 Diagrams of the APMOVPE reactor vessel, including: (a) A side view of the complete reactor vessel revealing the gas flow pattern and major components. (b) A top view of the specially designed reactor vessel inlet. (c) A top view through a section directly above the susceptor showing the gas flow pattern. (d) An oblique view of the reactor vessel top.

of studying the flow pattern, streamline visualization experiments were performed using a mixture of $TiCl_4$ and H_2O vapors injected upstream of the reactor inlet at room temperature which react to form TiO_2 particles. The gas flow pattern was studied visually as a function of the gas flow rate and the susceptor temperature by selectively illuminating sections of the reactor using a collimated light source with the laboratory room lights turned off. Gas flow streamlines are easily observed under these conditions due to optical scattering from the TiO_2 particles. With this technique, it was determined that the flow pattern is as shown in Figures 3.2 (a) and (c). Upon encountering the susceptor, gas flow separation takes place at the susceptor edge causing a portion of the gas stream to flow radially inward across the top face of the susceptor. Due to the original rotational motion imparted by the tangential inlets, the gas flow pattern across the substrate is presumed to be as shown in Figure 3.2 (c) (this was difficult to observe directly). Once the flow pattern is fully developed, a toroidal flow cell is formed above the susceptor surface as illustrated in cross section in Figure 3.2 (a). Figure 3.2 (d) gives an oblique view of the reactor top with a substrate situated on the susceptor.

Two extremely important effects occur as a result of the flow pattern characteristics: i) The spiraling inward radial flow across the substrate surface leads to remarkably uniform epilayers, both in thickness and composition. This can be explained, at least partially, by the fact that the nutrient vapor phase above the substrate encounters a decreasing substrate area as it travels across and becomes depleted. Furthermore, since the gas flow is substantially parallel to the substrate surface one would expect the stagnant boundary layer to be uniform thereby promoting uniform growth. ii) The toroidal flow cell established above the susceptor at room temperature has characteristics which follow the natural convective flow patterns once the susceptor is heated. As gases travel radially inward across the hot susceptor, there is a tendency for the gases to rise due to bouyancy effects. This behavior tends to reinforce the flow pattern observed at room temperature. Indeed, when performing the streamline

visualization experiments the flow pattern remained stable from room temperature up to a susceptor temperature of 1000°C. This remarkable flow pattern stability is extremely useful since it implies that the deposition characteristics should be relatively insensitive to changes in the growth temperature. A similar stability was observed with respect to the gas flow rate into the reactor.

Epilayers uniform to within ±3% are grown with this reactor on a routine basis. The ability to grow highly uniform structures was of paramount importance to this work since direct comparisons between different grading structures and the associated device results would have been meaningless otherwise. Figures 3.3 and 3.4 give examples of the degree of $GaAs_{1-x}P_x$ epilayer thickness and compositional uniformity typically achieved, respectively. Further evidence of high epilayer uniformity is shown in the solar cell performance data discussed in subsection 4.3.

3.2.3 Epitaxial Growth Procedure

The growth procedure consisted of a number of steps including substrate preparation, reactor preparation, pre-growth purging of the reactor, thermal desorption of the surface oxide on the substrate, growth of the heterostructure and post-growth cooling and flushing of the reactor.

Single-crystal p^+-GaAs substrates oriented (100) 2° toward the (110) and doped with Zn to give a room-temperature hole concentration of ~ 1×10^{19} cm^{-3} were prepared for growth by cleaving to the desired size (usually 1 cm x 1.5 cm), degreasing in a sequence of electronic-grade solvents (trichloroethylene (TCE), acetone (ACE), isopropyl alcohol (IPA), blow dry with N_2), etching in a solution of 6 H_2SO_4: 1 H_2O_2: 1 H_2O at 35°C for 2 minutes, rinsing in

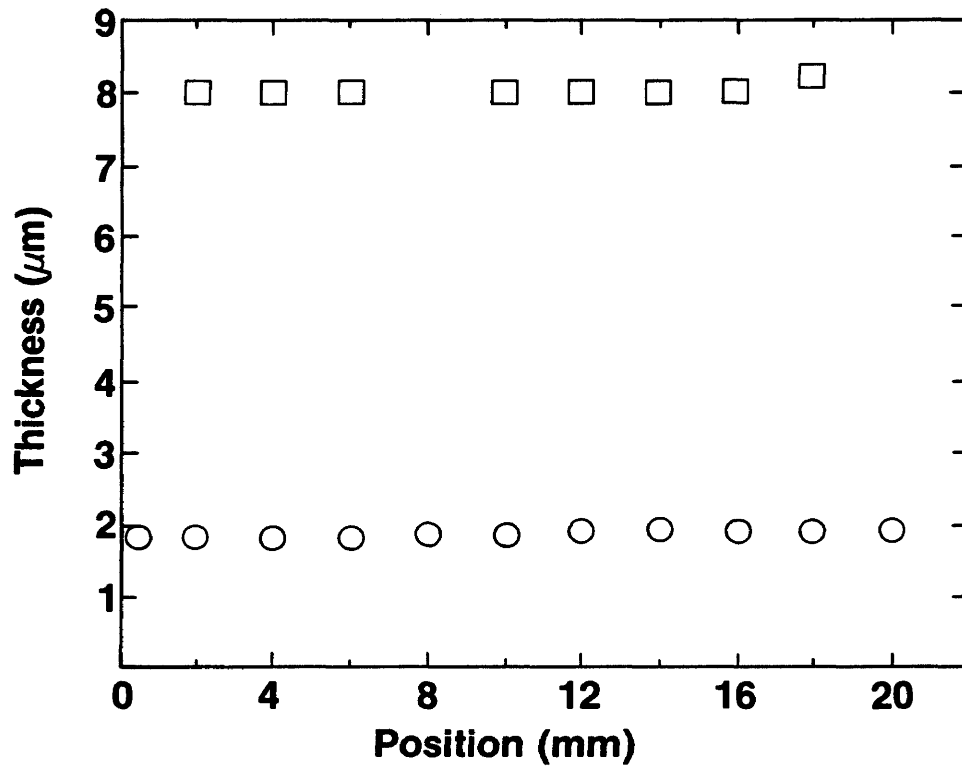

Figure 3.3 Typical thickness profiles for $GaAs_{1-x}P_x$ epilayers grown on 2cm x 2cm GaAs substrates.

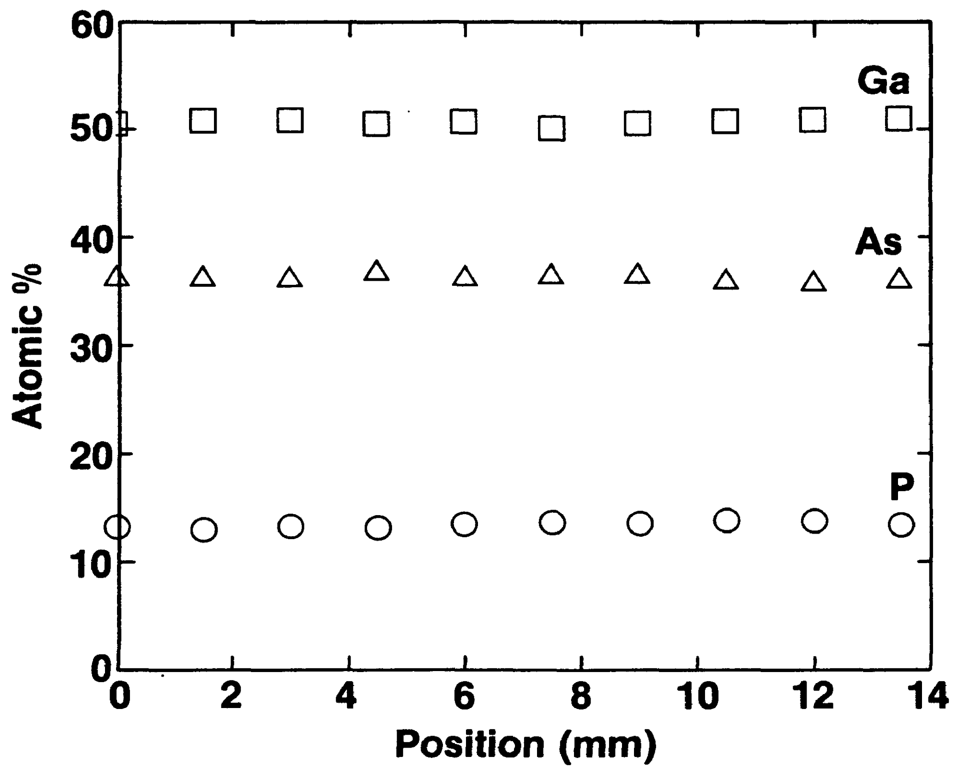

Figure 3.4 EPMA surface composition profile for a typical $GaAs_{0.74}P_{0.26}$ epilayer.

deionized (D.I.) H_2O and blowing dry with dry N_2. The etching procedure is designed to remove any residual sub-surface damage in the wafer due to polishing by the vendor and leaves a remaining oxide layer which is volatile at high temperatures.

A freshly cleaned reactor vessel was used for each growth run. Deposition on the quartz reactor walls from a previous growth run was removed using aqua regia (3 conc. HCl: 1 HNO_3) at room temperature followed by a thorough rinse in D.I. H_2O. The reactor halves were then dried in an oven in air at 120°C for at least 2 hours prior to using for growth. Similarly, the susceptors were vapor etched using gaseous HCl (5 sccm) in an H_2 carrier flow (1 slpm) at 900°C for about 15 minutes in order to provide a thorough bakeout and to remove any previous deposition.

After loading the substrate, the reactor was flushed with H_2 for about 20 minutes using the same flow rate used during growth (3 slpm). AsH_3 (10 sccm) was then introduced into the reactor in order to provide an arsenic over-pressure and the susceptor temperature was raised to 750°C for about 15 minutes to thermally desorb the oxide layer on the substrate surface.

A listing of the conditions used during the growth process is given in Table 3.2. Epilayer growth was initiated by introducing $(CH_3)_3Ga$ into the reactor, with the addition of $(C_2H_5)_2Zn$ for p-type doping, thus forming the p^+-GaAs buffer layer. Growth proceeded in a continuous manner and the phosphorus mole fraction in the compositionally graded region was controlled by varying the PH_3 flow rate while keeping the AsH_3 flow rate constant in accordance with the data presented in sub-subsection 4.2.2. A relatively high temperature (750°C) was used during growth in order to increase the efficiency of P incorporation in the solid phase as described in sub-subsection 4.2.2. Formation of the n^+/p SHJ in the upper layer

Table 3.2 APMOVPE growth conditions and reactor performance characteristics for $GaAs_{1-x}P_x/GaAs$ epitaxial heterostructures.

Parameter	Value
Reactor pressure	640 mm Hg
Growth temperature	750 °C
Growth rate	6 $\mu m\ hr^{-1}$
Hydrogen carrier flow rate	3000 sccm
[Group V]/[Group III] in vapor	29.5 - 56.8
$(CH_3)_3Ga$ mole fraction	1.08×10^{-4}
$(C_2H_5)_2Zn$ mole fraction (p^+-layer)	3.94×10^{-6}
$(C_2H_5)_2Zn$ mole fraction (p-layer)	3.94×10^{-7}
H_2Se mole fraction (n^+-layer)	7.58×10^{-6}
Epilayer uniformity	±3% variation
Heterointerface transition width	15 Å

of constant composition was achieved by adding H_2Se to the reactor carrier flow while simultaneously deleting the $(C_2H_5)_2Zn$. The metallurgical junction depth was assumed to be equal to the time interval between introduction of H_2Se and termination of growth multiplied by the growth rate determined from measurements made on thick layers. Growth was terminated by deleting the $(CH_3)_3Ga$ and H_2Se flows to the reactor while retaining the AsH_3 and PH_3 flows in order to maintain the epilayer integrity during cooldown. Following cooldown, the AsH_3 and PH_3 flows were deleted from the reactor and the reactor was flushed with H_2 at a flow rate of 3 slpm for at least 15 minutes prior to unloading the epiwafer.

3.3 $GaAs_{0.74}P_{0.26}$ Solar Cell Fabrication

Following growth, the epitaxial structures were processed using standard photolithographic and wet-chemical etching techniques to form arrays (5 - 10 devices) of electrically isolated mesa solar cells each with a total area of 0.10 cm^2 and a front grid coverage of about 12%. The sequence of processing steps listed below was typically employed:

1) Cleave epiwafer to desired size.
2) Affix the epiwafer face down on a glass microscope slide using Apiezon black wax while leaving the back surface exposed. The black wax melts on a hot plate at 90-100°C. This leaves the front surface of the wafer protected in order to perform the next step.
3) Etch the back surface of the wafer in a solution of 6 H_2SO_4: 1 H_2O_2: 1 H_2O at room temperature for 5 minutes. This solution etches GaAs at ~ 0.4 μm $min.^{-1}$ and thereby removes any inadvertant growth on the back surface of the wafer which might interfere in the formation of an ohmic contact.
4) Rinse the wafer/slide combination thoroughly in deionized H_2O and blow dry in dry N_2.
5) Form an ohmic back contact to the p^+-GaAs wafer by electroplating about 1 μm of Au to

the back surface of the wafer. Aurovil UP-24 Au plating solution is used at 60°C for this purpose with a plating current density of 15 $mAcm^{-2}$.

6) Rinse the wafer/slide combination thoroughly in D.I. H_2O and blow dry in dry N_2.

7) Remove epiwafer from slide by heating to 100°C on a hot plate and pushing off slide. Remove wax on wafer using a sequence of organic solvents including TCE, ACE and IPA using a steady stream dispensed from a squirt bottle. The sample should not be allowed to dry until the final rinse with IPA is completed to ensure that a residue is not left on the wafer surface. Blow dry with dry N_2.

8) Spin Shipley S1400-32 positive photoresist onto the wafer front surface (5000 rpm, 30 sec.).

9) Soft-bake the photoresist (85°C, 30 min.)

10) Expose front grid metallization patterns in the photoresist and develop.

11) Coat back surface and edges of wafer with photoresist, leaving a corner of the back contact exposed for an electroplating contact. Soft-bake the photoresist. This procedure electrically insulates the back contact and wafer edges thus allowing the front contacts to be electroplated in the next step.

12) Electroplate the Au front grid contacts to a thickness of 6 µm using the Aurovil plating solution mentioned above. Make sure to keep the plating contact to the back surface of the wafer out of the plating solution such that all of the plating occurs at the front grid patterns.

13) Rinse the wafer thoroughly in deionized H_2O and blow dry in dry N_2.

14) Remove the photoresist by rinsing in ACE followed by IPA and then blow dry in dry N_2.

15) Spin positive photoresist onto the wafer front surface.

16) Soft bake the photoresist.

17) Align and expose the solar cell isolation moat (mesa) patterns in the photoresist and develop.

18) Chemically etch the isolation moats using the 6 H_2SO_4: 1 H_2O_2: 1 H_2O solution at room

temperature for 30 seconds. This procedure forms the individual mesa solar cells, thus providing two important functions: a) it electrically isolates the solar cells, and b) it defines the total area of each cell.

19) Remove the photoresist by rinsing in ACE followed by IPA and then blow dry in dry N_2.

At this point, the solar cells are completed and ready for characterization. Typically, antireflection coatings (ARC) are applied to solar cells in order to maximize the amount of light absorbed in the cell. However, for the purposes of this study, the cells were evaluated without ARC's in an effort to keep the cell processing and data analysis as simple as possible. A finished array of $GaAs_{0.74}P_{0.26}$ SHJ solar cells processed on a typical epiwafer is shown in plan view in Figure 3.5.

Following step 14 above, the grid-to-grid resistance between adjacent grids was evaluated for each of the epiwafers. The resistance was found to be slightly higher (less than a factor of 2) for samples with fewer grading steps, however, the grid-to-grid J-V characteristic was ohmic for all samples. It is presumed that the contact resistance is the same for all of the samples and that the increase in grid-to-grid resistance observed for the more coarsely graded samples is due to a reduction in the majority carrier mobility in the emitter layer as a result of a higher defect density, thus leading to an increased emitter sheet resistance.

3.4 Material/Device Characterization

Several different characterization techniques were employed in studying the details of the $GaAs_{1-x}P_x$/GaAs heterostructures and the performance of the resulting $GaAs_{0.74}P_{0.26}$ solar cells. The various techniques and their application are listed in Table 3.3. One of the advantages of performing such a study at SERI is the wide spectrum of analytical techniques

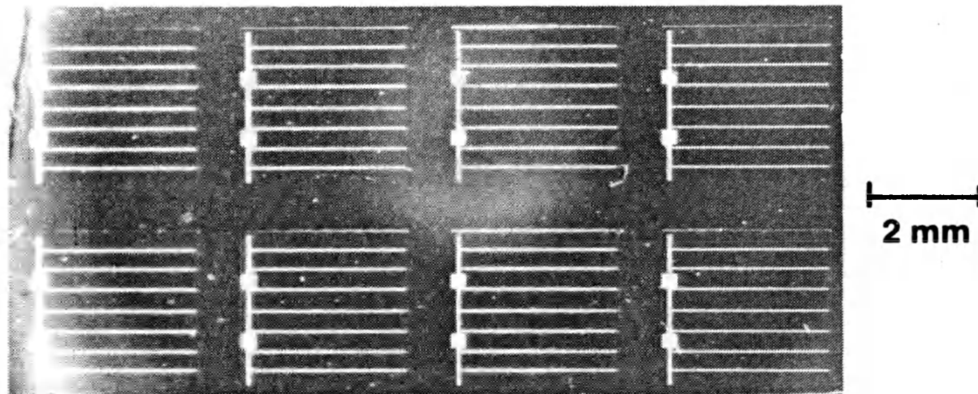

Figure 3.5 Photomicrograph of a finished $GaAs_{0.74}P_{0.26}$ solar cell array fabricated on a GaAs wafer, as viewed from above. The front grid contacts and individual device mesas are visible.

Table 3.3 Material/device characterization techniques used to investigate the $GaAs_{1-x}P_x/GaAs$ solar cell structures.

Characterization technique	Information obtained
Optical Microscopy	Surface morphology, layer thickness and morphology
Electron Probe Microanalysis (EPMA)	Material composition
Electron Beam Induced Current (EBIC)	Defect type, density and morphology
Junction Capacitance *vs* Voltage (C-V)	p-layer impurity concentration
Transmission Electron Microscopy (TEM)	Defect type, density and morphology
Dark Current Density *vs* Voltage (DJV)	p-n junction parameters
Illuminated Current Density *vs* Voltage (IJV)	Solar cell performance parameters
Spectral Response	Quantum efficiency as a function of wavelength

available, especially with respect to semiconductor materials characterization and photovoltaic device performance measurements. The individuals at SERI responsible for contributing to this work in these areas are indicated in the acknowledgements section along with their area of specialization.

The analytical techniques can be broken down into two rough categories; those relating to materials properties and those which quantify junction quality and solar cell performance, with some overlap existing for some of the techniques. Overall, it was intended that the heterostructures and related cells be analyzed in a manner consistent with establishing correlations between the grading parameters and the resulting materials properties and cell characteristics, thus satisfying the objectives orignally established for the project. Summarized in the sections which follow are the results obtained using such techniques.

4.0 RESULTS AND DISCUSSION

4.1 Introduction

A total of 10 heterostructures were grown for this study. Table 4.1 lists the grading parameters used in each of the samples as defined earlier in subsection 1.2. The thickness data given in Table 4.1 are nominal values, whereas the compositional data are based on actual measured values as discussed in sub-subsection 4.2.2 below.

In the final comparison of the solar cell performance results, the data obtained from samples 3 and 6 were eliminated from consideration for reasons which shall be described. However, this did not have an adverse effect on the final results and conclusions. The grading parameters in sample 7 were repeated in sample 8 in order to confirm unusual results originally observed in the solar cell IJV data for sample 7.

4.2 Properties of $GaAs_{1-x}P_x$/GaAs Epitaxial Device Structures

4.2.1 Morphology of Surfaces and Interfaces

Surface and heterointerface morphology was examined using a Zeiss Axiomat optical microscope with Nomarski inteference contrast capabilities. The surfaces were viewed in plan view in the as-grown state, whereas the interfaces were observed in cross section by cleaving the crystals along the (110) direction and then dipping the freshly cleaved edges in a delineation etchant consisting of equal parts of saturated aqueous solutions of potassium hydroxide and potassium ferricyanide. This was done for only a few seconds at room temperature and the samples were then rinsed in D.I. H_2O and blown dry in dry N_2. The

Table 4.1 Characteristics of the compositional grades in each of the $GaAs_{1-x}P_x/GaAs$ epitaxial heterostructures.

Sample	Grading Parameters	Δt_{st} (μm)	Δx_{st}	$(\Delta a/a)$ at first step (%)
1	Continuous t = 8 μm	G = 3.3 mole% P μm^{-1}		
2	n = 10 t = 9 μm	1.00	0.027	0.096
3	n = 7 t = 8 μm	1.33	0.036	0.129
4	n = 5 t = 8 μm	2.00	0.053	0.189
5	n = 5 t = 4 μm	1.00	0.054	0.193
6	n = 4 t = 8 μm	2.67	0.053	0.189
7	n = 3 t = 8 μm	4.00	0.087	0.311
8	n = 3 t = 8 μm	4.00	0.089	0.318
9	n = 2 t = 8 μm	8.00	0.125	0.446
10	n = 1 t = 0	0	0.274	0.978

samples were then mounted on a special sample holder with the cleaved and etched edges facing up and horizontal.

Photomicrographs of the sample cross sections as a function of the grading parameters are shown in Figure 4.1. A similar micrograph composite is given in Figure 4.2 for the sample surfaces. The cross sectional micrographs show that the interfaces in the step grades are sharp and planar and that the intended layer thicknesses have been achieved. From Figure 4.2, however, it is evident that two distinct trends in the surface morphology occur as the grading parameters are varied. For the continuous grade and the $n = 5$, $t = 8$ μm grade, the morphologies are essentially identical, as were results for $n = 4, 7, 10$, $t = 8\text{-}9$ μm grades not shown. The surfaces for these grades have a very fine , regular cross-hatched morphology and are virtually indistinguishable from grade to grade. Thus, it appears that the surface morphology is independent of the grading parameters for $n \geq 4$, $t \geq 8$ μm. As t is reduced from 8 μm to 4 μm, the surface retains a finely cross-hatched character however the cross hatch density appears to increase. A striking transition in the morphology occurs as n is reduced to 3. Rough, irregular surface features are observed on a cross-hatched backgound. As n is further reduced, the surface becomes rougher still, with the sample having no graded region exhibiting the roughest surface. It is interesting to note that microcracks were not seen on the surfaces of any of the structures despite the fact that the epilayers are in considerable biaxial tension. This result contradicts the general conclusions of Olsen, however the rough surfaces seen for the coarser grades corroborate his findings [13]. Overall, it is observed that the surface morphology appears to be dictated by the choice of grading parameters. Correlations between the surface effects and the dislocation density and morphology are discussed in sub-subsection 4.2.3.

It was mentioned earlier that the solar cell results from sample 3 were eliminated from

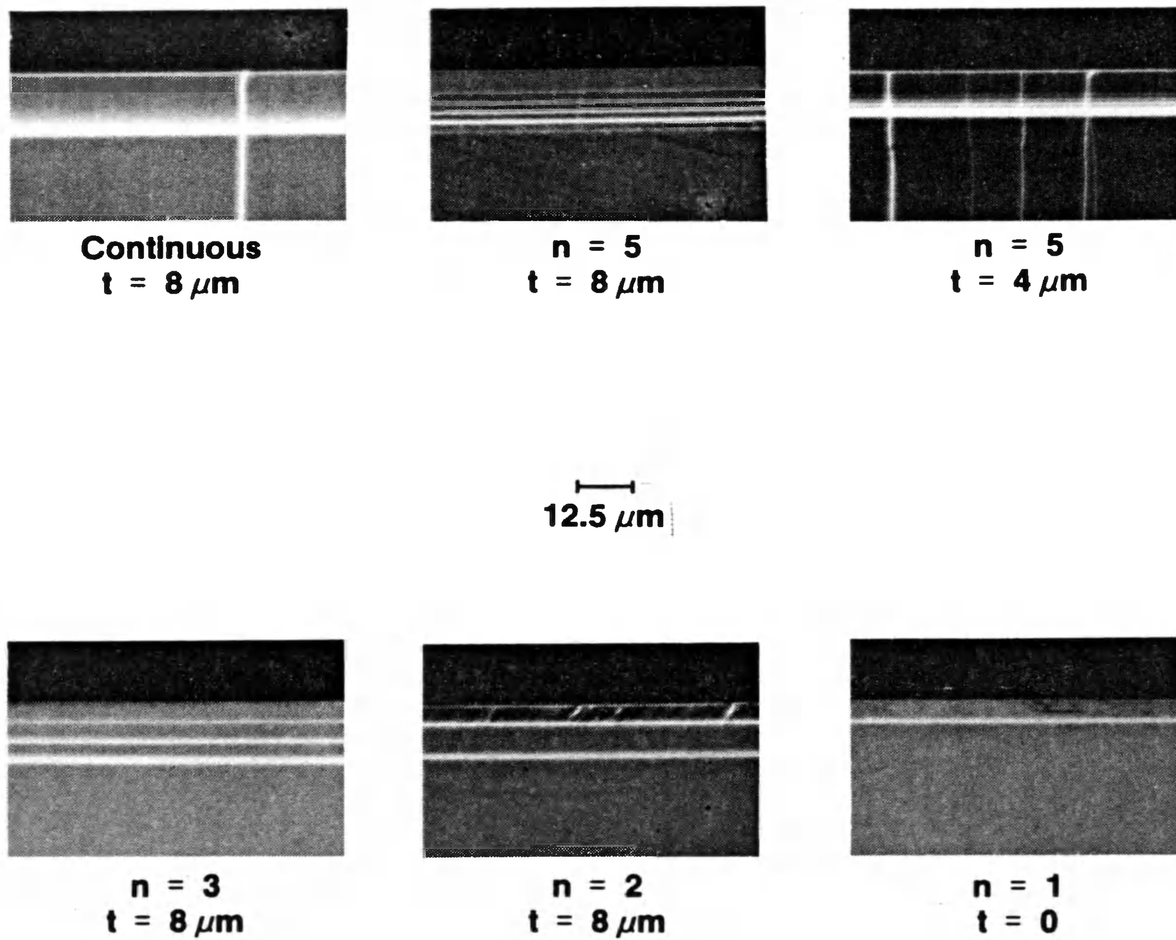

Figure 4.1 Photomicrographs of six different compositionally graded $GaAs_{1-x}P_x/GaAs$ heterostructure cross sections, with the grading parameters for each listed below.

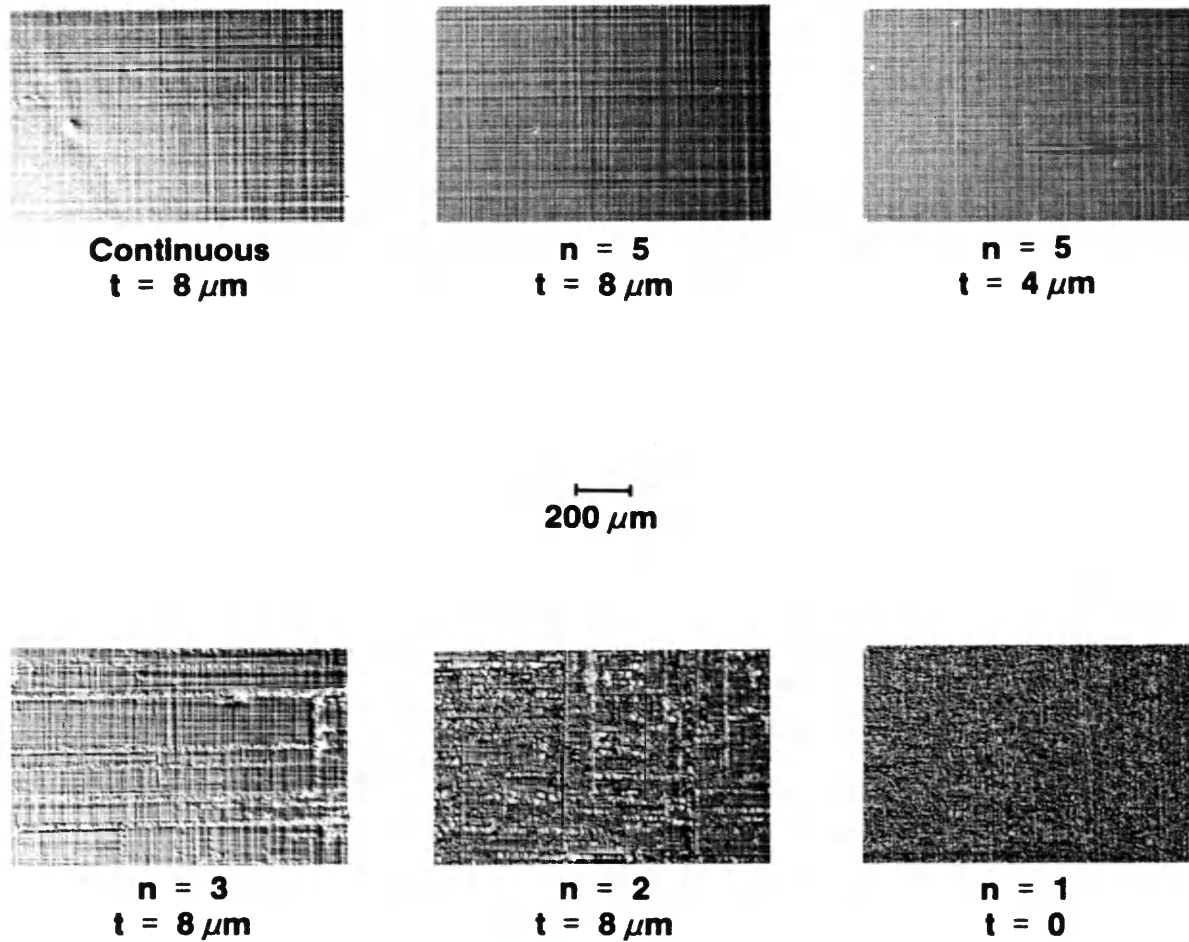

Figure 4.2 Photomicrographs of surface morphology as a function of the grading parameters.

the final cell performance analysis. Figure 4.3 shows photomicrographs of surface defects on sample 3 which apparently resulted from contamination of the substrate surface prior to growth. The substrate used to grow this sample was prepared and stored (covered) in a clean-air hood for 18 days prior to use, nevertheless, surface contamination occurred somehow during this unusually long storage period. Substrates for the other samples were all prepared and used within a few days and surface defects were not observed. V_{oc} values for cells processed on sample 3 were about 50 mV lower than the V_{oc}'s for cells on other samples with similar surface morphologies and crystalline defect densities. Apparently, the surface defects behave as shunt paths through the junction thus lowering V_{oc}. Despite rejection of the cell results, the compositional and crystalline defect density data from sample 3 were useful and the lost cell data are not believed to be critical due to the similarity of sample 3 with other samples having nearly identical grading parameters.

4.2.2 Compositional Analysis

Control and uniformity of the $GaAs_{1-x}P_x$ epilayer composition was an extremely important factor for this study since both the bandgap and the lattice constant vary with x. Therefore, an extensive compositional analysis was performed on each of the samples prepared for this work in order to confirm the validity of a comparative analysis of the solar cell results. Additionally, the compositional data provides a necessary basis for controlling and characterizing the growth process.

Epilayer composition was determined using EPMA with an electron beam voltage of 15 kV. The composition in the solar cell layers was of primary concern due to the effect on the bandgap. Table 4.2 gives a summary of EPMA data taken along the surface and a cleaved cross section for the cell layers in each sample. The data indicate that the composition is

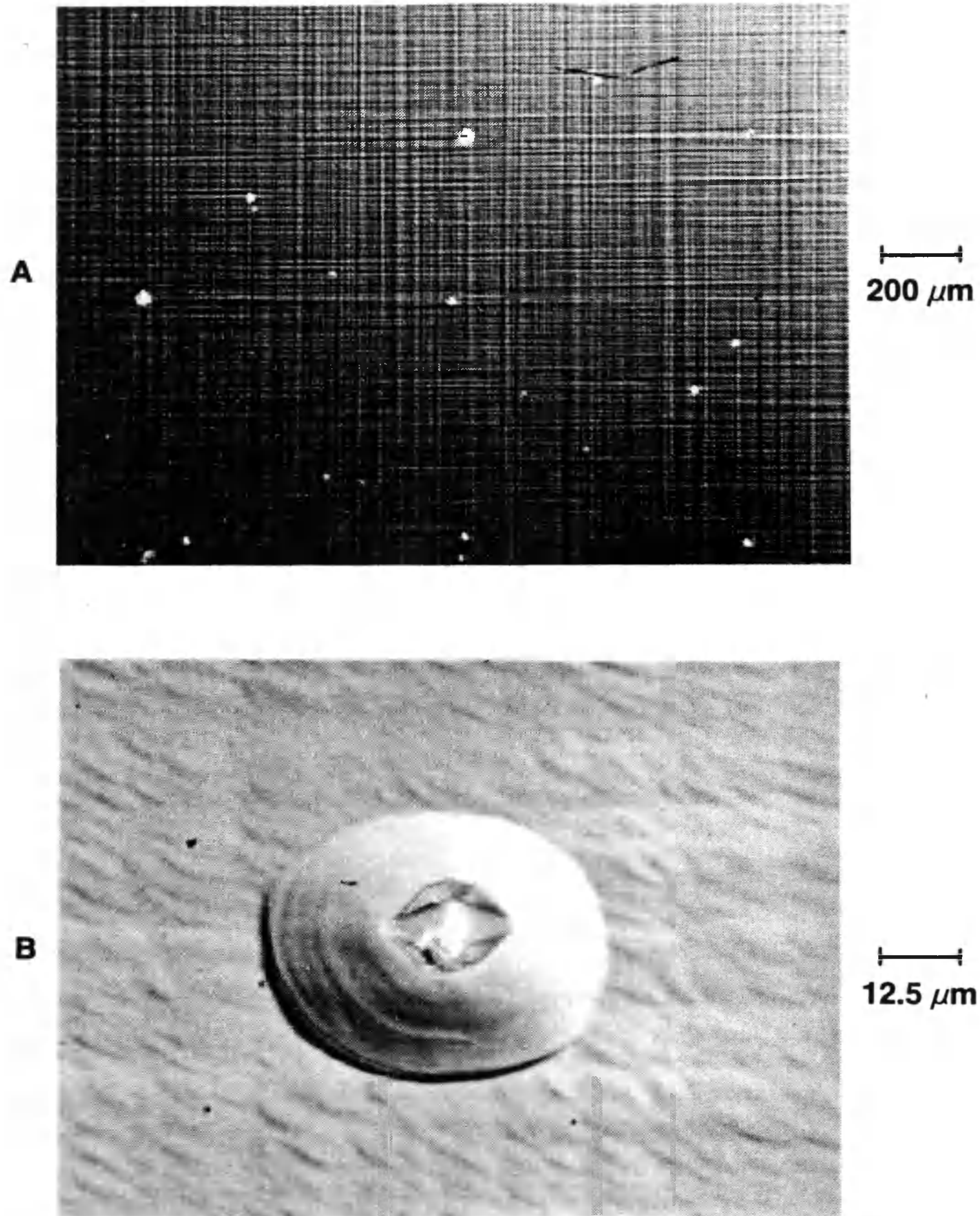

Figure 4.3 Photomicrographs of growth defects observed on the surface of sample 3 (n = 7, t = 8 μm) shown at (a) low, and (b) high magnification.

Table 4.2 EPMA solar cell layer compositional data summary for all $GaAs_{1-x}P_x$ samples grown in this study.

Sample	Grading Parameters	EPMA Surface Scan Data			EPMA Cross Section Scan Data		
		$\langle x \rangle \pm \sigma$	E_g (eV)	λ (nm)	$\langle x \rangle$	E_g (eV)	λ (nm)
1	Cont., t = 8 μm	0.261 ± 0.005	1.74	713	0.269	1.75	709
2	n = 10, t = 9 μm	0.275 ± 0.007	1.76	704	0.282	1.77	701
3	n = 7, t = 8 μm	0.249 ± 0.005	1.73	717	0.257	1.73	717
4	n = 5, t = 8 μm	0.267 ± 0.006	1.75	709	0.271	1.75	709
5	n = 5, t = 4 μm	0.270 ± 0.005	1.75	709	0.272	1.75	709
6	n = 4, t = 8 μm	0.211 ± 0.006	1.68	738	0.233	1.71	725
7	n = 3, t = 8 μm	0.262 ± 0.006	1.74	713	0.275	1.76	704
8	n = 3, t = 8 μm	0.266 ± 0.006	1.75	709	0.266	1.75	709
9	n = 2, t = 8 μm	0.250 ± 0.006	1.73	717	0.265	1.74	713
10	n = 1, t = 0	0.274 ± 0.012	1.76	704	0.280	1.76	704

extremely consistent from sample to sample (with the exception of sample 6) and that the standard deviation for the surface scan data is very small which indicates a high degree of lateral uniformity. The surface scan and cross section scan data are in good agreement despite the fact that only a few data points were taken along a cross section due to the layer thickness (i.e., only 5 μm). Among the samples used for comparison of the cell results, the bandgaps agree to within ± 0.015 eV or, in terms of wavelength, ± 6.5 nm. Overall, the average P mole fraction for these samples is 0.264, which corresponds to a bandgap of 1.74 eV or 713 nm, and the maximum lateral variation in x on any sample is ±3%. The conversion from energy to wavelength is obtained using the following equation

$$\lambda E = hc = 1239.9 eVnm \qquad 4.1$$

Sample 6 has a cell layer P mole fraction that is substantially lower than the other samples and, therefore, was not considered in the final cell performance comparison. After reviewing the growth procedures used for this sample, it was discovered that a susceptor with a slightly higher retaining lip was used for the growth. This change in reactor geometry in the vicinity of the growing surface, albeit an ostensibly minor one, apparently had a significant effect on the growth chemistry, resulting in a lower value of x. The relationship and sensitivity of the relative incorporation of P and As in the solid as a function of reactor geometry is illustrated by this result.

Cross sectional EPMA scans were also useful in monitoring the different grading schemes which were grown. Examples of such data for a continuous grade (sample 1) and a step grade (sample 7) are shown in Figures 4.4 and 4.5, respectively. The data show the expected features for these samples.

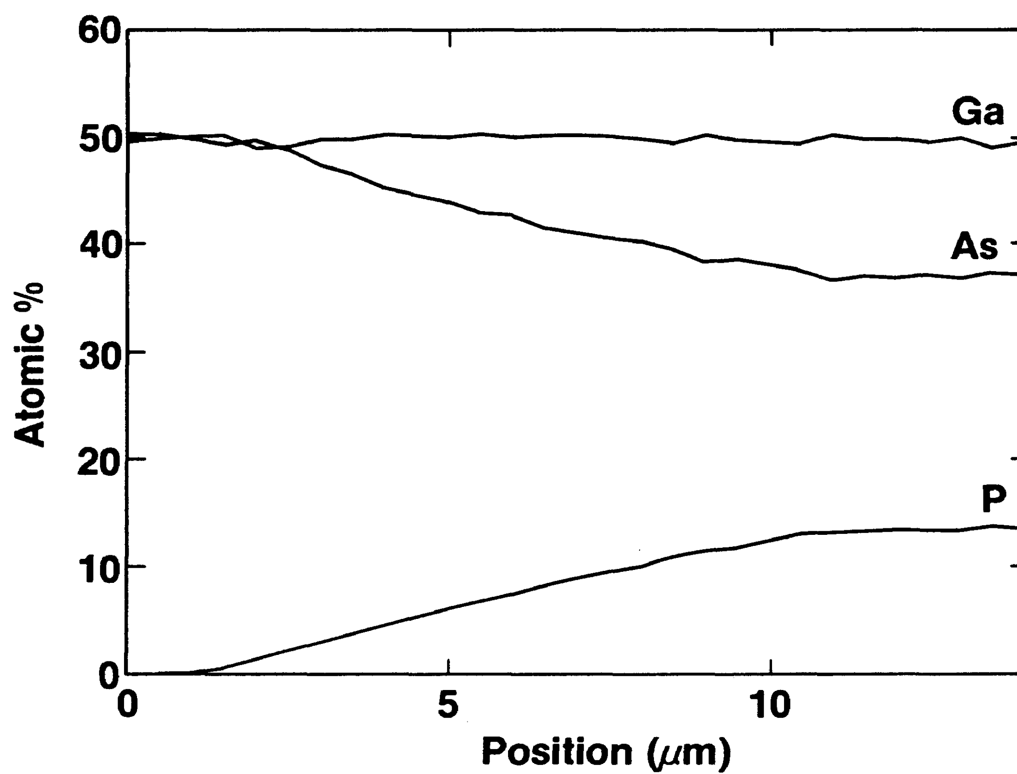

Figure 4.4 EPMA cross sectional composition profile for a continously graded $GaAs_{1-x}P_x$/GaAs heterostructure (sample 1, continuous, t = 8 μm).

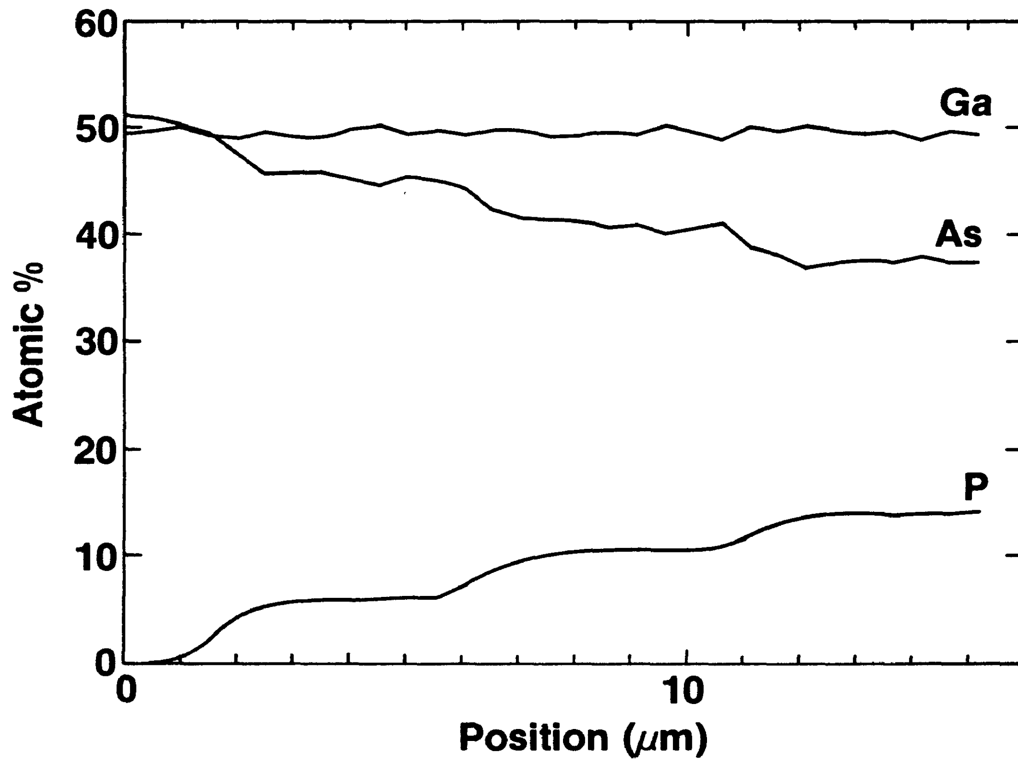

Figure 4.5 EPMA cross sectional composition profile for a step graded $GaAs_{1-x}P_x$/GaAs heterostructure (sample 7, n = 3, t = 8 μm).

In the growth of $GaAs_{1-x}P_x$ by MOVPE using AsH_3 and PH_3 as group V precursors, it is generally found that the solid-phase composition differs from that of the nutrient vapor phase due to a redistribution of the P-to-As ratio. Several researchers have reported on this phenomenon and have shown that the solid phase is always P-deficient with respect to the vapor due to a preferential incorporation of As in the solid [33 -35]. The exact details of the mechanism(s) governing this effect are not completely known, however it is believed to be related to processes occurring during the heterogeneous decomposition of the hydrides on the substrate surface.

Generally, the redistribution of the P-to-As ratio between the vapor and solid phases depends on a number of factors including the growth temperature, reactor geometry, total concentration of hydride species and the substrate orientation. The incorporation of P relative to As is strongly temperature dependent and increases sharply with increasing growth temperature. Under the growth conditions used in this work, the above-mentioned parameters can all be taken as constant from run to run and during growth (the total hydride concentration varies during a run, but over a small range) and an empirically derived P vapor/solid distribution coefficient defined by the following expression

$$\frac{x}{1-x} = K_P \frac{f_{PH_3}}{f_{AsH_3}} \qquad 4.2$$

can be used to relate the vapor phase composition to that obtained in the solid. Thus, from equation 4.2 it is clear that the value of K_p gives a quantitative measure of the incorporation efficiency of P in the solid relative to As. The mole fraction of P in the vapor is given by

$$x_v = \frac{f_{PH_3}}{f_{PH_3} + f_{AsH_3}} \qquad 4.3$$

Therefore, the mole fraction of P in the solid as a function of the mole fraction of P in the vapor is given by the following expression

$$x_s = \frac{x_v K_P}{1 + x_v(K_P - 1)} \qquad 4.4$$

Thus, once K_p is known, the vapor composition can be tailored to yield a desired solid composition.

In Table 4.3, a summary of the vapor/solid compositional data for the samples prepared in this study is given along with the corresponding parameter values used to calculate K_P. Cross-sectional analysis by EPMA of individual layers in step-graded regions which were sufficiently thick allowed intermediate vapor/solid compositions to be evaluated. According to equation 4.2 above, and as shown in Figure 4.6, K_p is determined to be 0.395 which indicates that As is incorporated in the solid phase more than twice as efficiently as P under the growth conditions used.

The sublinear behavior of x_s as a function of x_v is illustrated in Figure 4.7. In this figure, the experimental data are plotted against a curve generated using equation 4.4 and good agreement is obtained. This type of vapor/solid compositional analysis is extremely useful since it provides an accurate means of obtaining an arbitrary solid composition and also partially elucidates the growth processes.

4.2.3 Defect Analysis

A combination of TEM (both cross sectional and plan view) and EBIC techniques were used to analyze the crystalline defects in the structures. Cross sectional TEM techniques are

Table 4.3 A summary of the vapor/solid compositional data used to determine x_s as a function of x_v. The parameters used to calculate the empirical P vapor/solid distribution coefficient K_P are also listed.

Sample	Grading Parameters	Layer	f_{AsH_3} (sccm)	f_{PH_3} (sccm)	f_{PH_3}/f_{AsH_3}	x_v	EPMA Cross Section Scan Data		EPMA Surface Scan Data	
							$\langle x_s \rangle$	$\langle x_s \rangle/(1-\langle x_s \rangle)$	$\langle x_s \rangle$	$\langle x_s \rangle/(1-\langle x_s \rangle)$
1	Continuous t = 8 μm	Junction	10	9.25	0.925	0.481	0.269	0.368	0.261	0.353
2	n = 10 t = 9 μm	Junction	10	9.25	0.925	0.481	0.282	0.393	0.275	0.379
3	n = 7 t = 8 μm	Junction	10	9.25	0.925	0.481	0.257	0.346	0.249	0.332
4	n = 5 t = 8 μm	1	10	1.85	0.185	0.156	0.068	0.073	-------	-------
		2	10	3.70	0.370	0.270	0.124	0.142	-------	-------
		3	10	5.55	0.555	0.357	0.179	0.218	-------	-------
		4	10	7.40	0.740	0.425	0.221	0.284	-------	-------
		Junction	10	9.25	0.925	0.481	0.271	0.372	0.267	0.364

Table 4.3 Continued...

Sample	Grading Parameters	Layer	f_{AsH_3} (sccm)	f_{PH_3} (sccm)	f_{PH_3}/f_{AsH_3}	x_v	EPMA Cross Section Scan Data		EPMA Surface Scan Data	
							$\langle x_s \rangle$	$\langle x_s \rangle/(1-\langle x_s \rangle)$	$\langle x_s \rangle$	$\langle x_s \rangle/(1-\langle x_s \rangle)$
5	n = 5 t = 4 μm	Junction	10	9.25	0.925	0.418	0.272	0.374	0.270	0.370
7	n = 3	1	10	3.10	0.310	0.237	0.117	0.133	-------	-------
	t = 8 μm	2	10	6.15	0.615	0.381	0.208	0.263	-------	-------
		Junction	10	9.25	0.925	0.481	0.275	0.379	0.262	0.355
8	n = 3	1	10	3.10	0.310	0.237	0.107	0.120	-------	-------
	t = 8 μm	2	10	6.15	0.615	0.381	0.197	0.245	-------	-------
		Junction	10	9.25	0.925	0.481	0.266	0.362	0.266	0.362
9	n = 2	1	10	4.65	0.465	0.317	0.152	0.179	-------	-------
	t = 8 μm	Junction	10	9.25	0.925	0.481	0.265	0.361	0.250	0.333
10	n = 1 t = 0	Junction	10	9.25	0.925	0.481	0.280	0.389	0.275	0.379

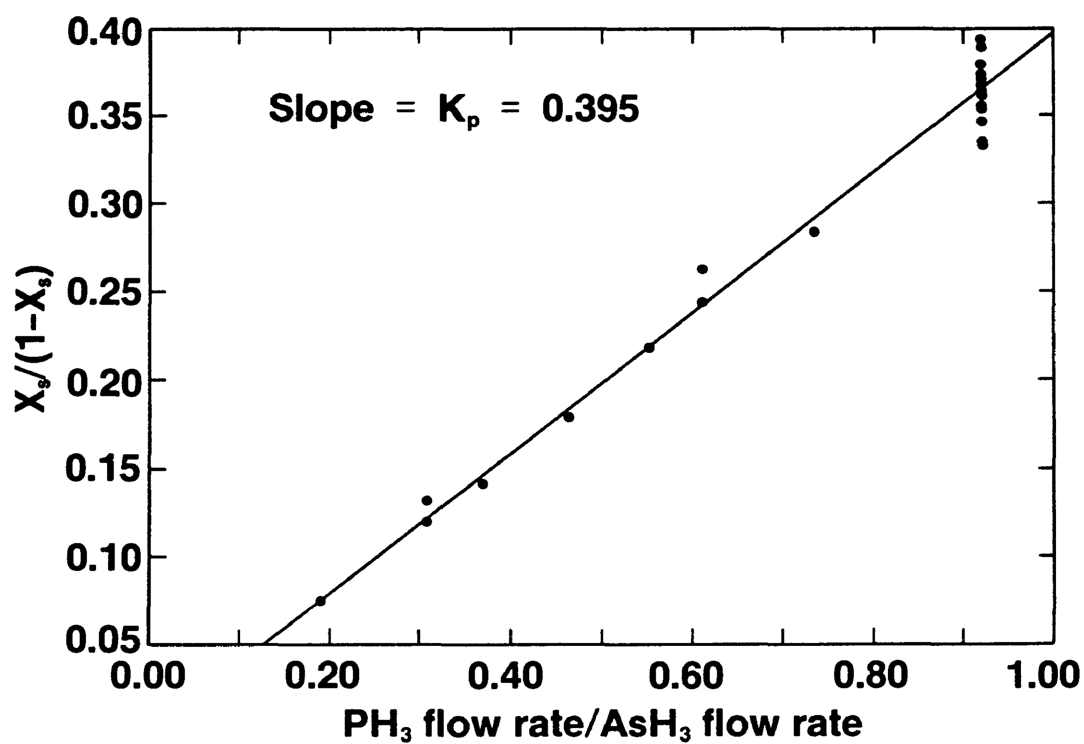

Figure 4.6 $x_s/(1-x_s)$ *vs* (PH_3 flow rate)/(AsH_3 flow rate), showing a least-squares fit to the experimental data. The slope of the.line gives the P vapor/solid distribution coefficient K_P.

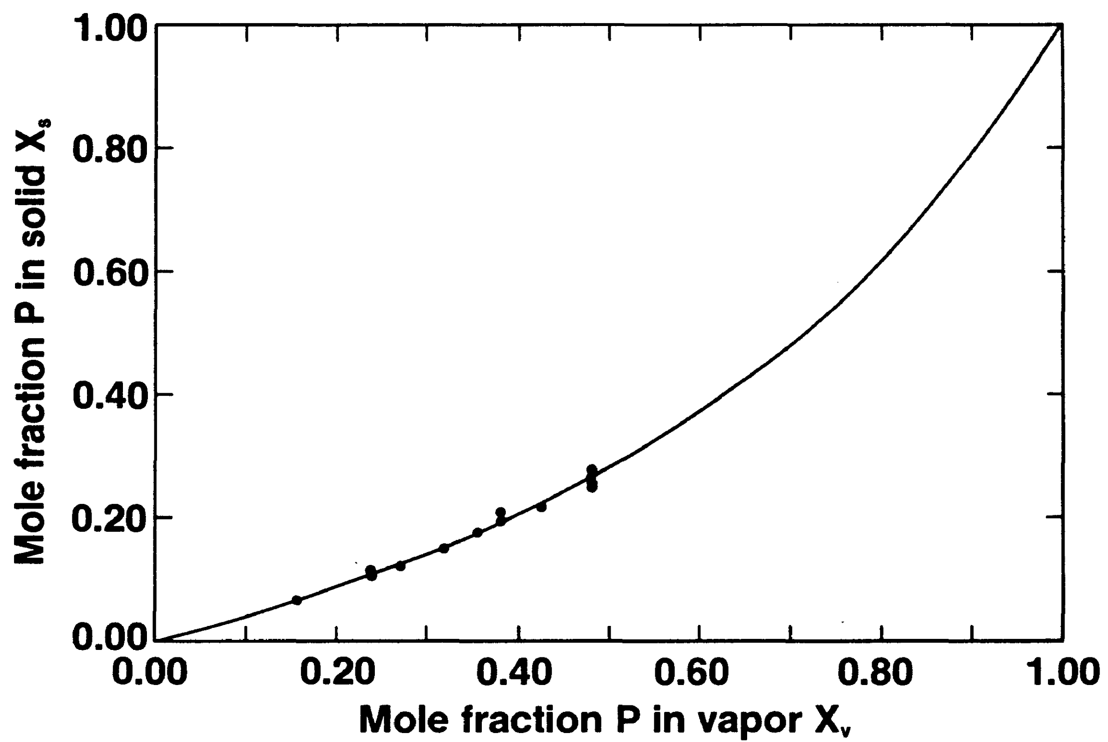

Figure 4.7 x_s *vs* x_v for $GaAs_{1-x}P_x$ epilayers grown under the conditions used in this study. The solid line fit was obtained using the empirically derived P vapor/solid distribution coefficient ($K_p = 0.395$).

useful for observing dislocation generation and propagation, whereas plan-view TEM allows for the quantification of high areal dislocation densities ($> 10^7$ cm^{-2}). Plan-view EBIC in conjunction with a scanning electron microscope (SEM) provides a means of determining electrically active defect densities which are below the detection limit for TEM ($< 10^7$ cm^{-2}). Additionally, the defect morphology can be observed over a wide area and as a function of depth in the sample by varying the electron beam voltage. For the EBIC analysis in this work, an electron beam voltage of 25 kV was used for all samples, resulting in a carrier generation volume 3-4 μm in diameter. Thus, the EBIC images generated in this manner reveal defects present in the solar cell layers only, and allow direct comparisons to be made between different structures. Of course, since the EBIC technique requires that the sample have a junction and electrical contacts, the measurements were performed directly on representative solar cells from each of the epiwafers.

In step graded structures, the generation and morphology of misfit dislocation networks and the generation and propagation of threading dislocations were each studied using cross sectional TEM. Figure 4.8 illustrates the dislocation morphology which is typically seen in such structures. In the vicinity of each compositional step, extensive, dense misfit dislocation networks form, with the extent and density of the network varying directly with the magnitude of the misfit or compositional increment at the step. Additionally, threading dislocations originating from a misfit network propagate through the graded region to a successive step where they are bent over into the misfit orientation (i.e., along <011> directions) as long as they are sufficiently inclined to the growth plane. However, the portion of the threading dislocations which align themselves along the [100] direction is unperturbed by the compositional steps and propagate directly into the solar cell layers at the surface. Therefore, the elimination of all threading dislocations from the cell layers is impossible by simply step grading. However, misfit dislocations can be eliminated from the cell layers by

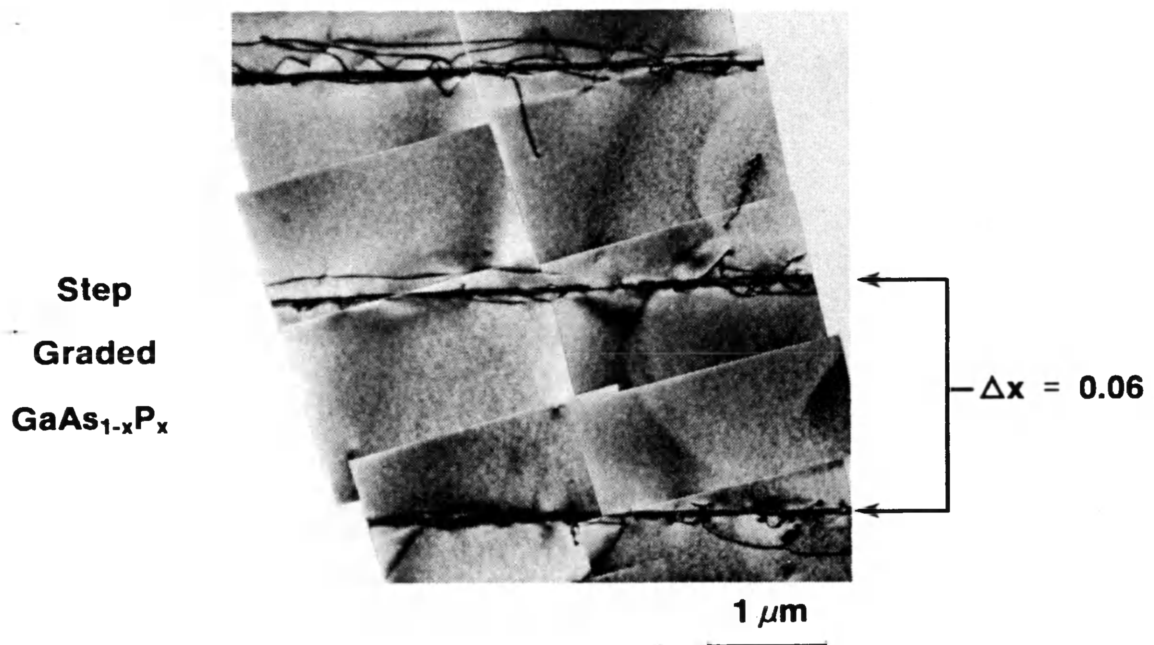

Figure 4.8 Cross sectional TEM montage of a compositionally step graded $GaAs_{1-x}P_x$ structure revealing dislocation networks in the vicinity of each compositional step.

keeping n and t sufficiently large, with n being the most critical parameter.

The cross sectional TEM results are corroborated by plan-view EBIC results shown in Figure 4.9. In this composite of micrographs, the density and morphology of electrically active defects in the cell layers is shown as a function of the grading parameters. Similar to what was observed for the cell layer surface morphologies, two trends in the dislocation morphology are seen as the grading parameters are varied. For the continuous grade and step graded structures with $n \geq 4$ and $t \geq 8$ µm, the defects observed in the cell layers primarily consist of a relatively low density of threading dislocations (dark spots in the EBIC micrographs) which are orthogonal to the growth plane. As t is reduced from 8 µm to 4 µm, D_T increases by a factor of 3 to 4, however misfit dislocations are still absent in the cell layers. However, as n is reduced to 3 the presence of a misfit dislocation network is clearly observed, appearing in the EBIC micrograph as thick, dark, perpendicular lines. The penetration of misfit dislocations into the cell layers is presumably due to the severity of the compositional step ($\Delta x_{st} = 0.087$) at the base of the SHJ p-layer for n = 3. As n is further reduced while keeping t = 8 µm, both D_T and D_M continue to increase, with sample 10 (n = 1, t = 0) exhibiting the highest defect density.

Based on these observations, it is concluded that a strong correlation exists between the cell surface morphology and the dislocation configuration in the cell layers for each set of grading parameters. A smooth, cross-hatched surface indicates that misfit dislocations are confined to layers well below the SHJ layers, whereas a rough, irregular surface clearly arises from the penetration of misfit dislocations well into the cell layers. In the next subsection, the effect on cell performance of the dislocation type, density and morphology is quantiifed and analyzed.

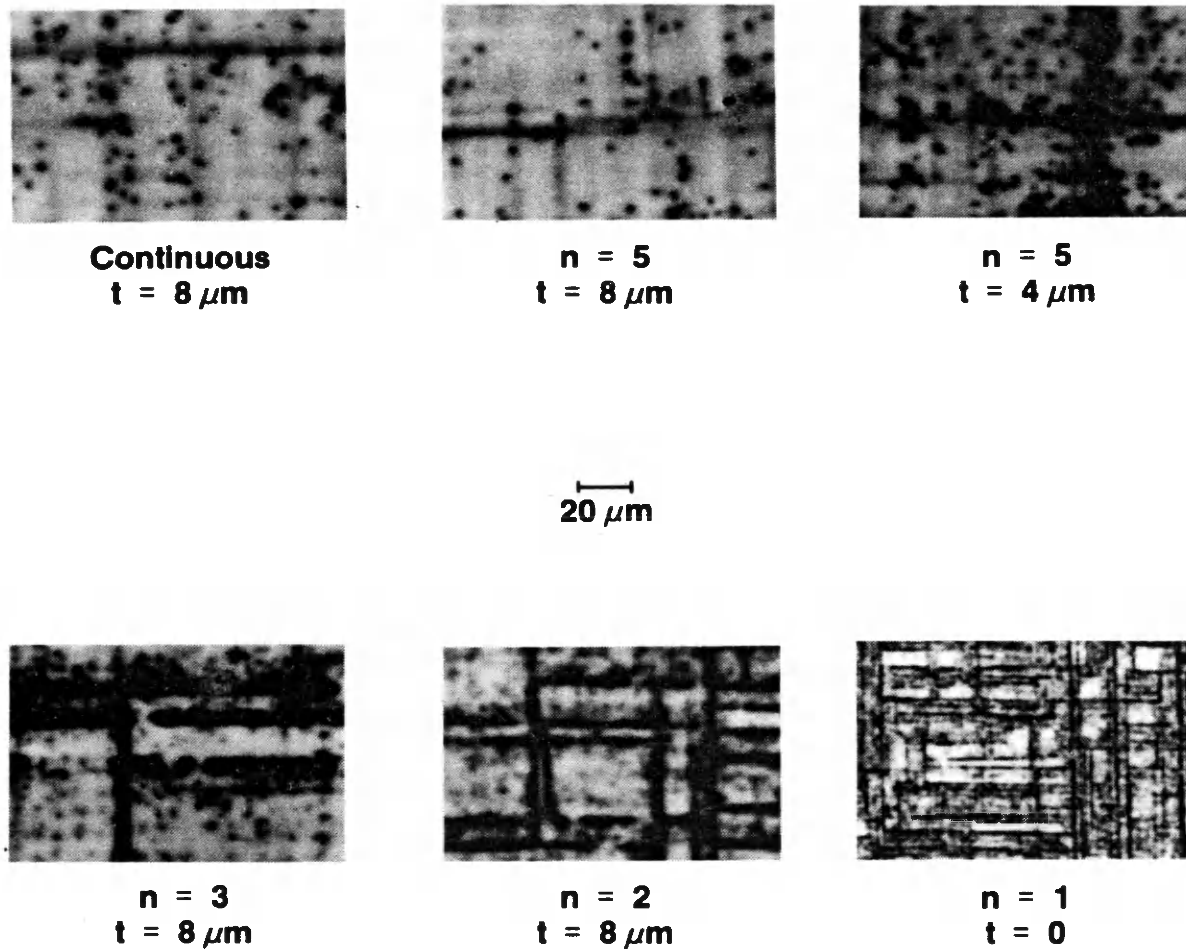

Figure 4.9 Plan-view EBIC micrographs revealing the dislocation density and morphology as a function of the grading parameters. The dark lines and spots correspond to dislocations where electron-generated minority carriers recombine.

4.3 $GaAs_{0.74}P_{0.26}$ Photovoltaic Device Characteristics

4.3.1 Illuminated J-V Characteristics

Illuminated J-V data for the solar cells were measured with respect to a direct normal spectrum (1000 Wm^{-2} total irradiance) while holding the junction temperature constant at 28°C. In calculating the cell conversion efficiency, the total junction area was used and the J-V data were corrected for spectral mismatch [36]. The measurement system incorporates a Spectrolab X-25 solar simulator and an automated HP-1000-based data acquisition system.

Table 4.4 gives a summary of the dislocation type and density and the IJV characteristics for the cells on each epiwafer as a function of the grading parameters. D_T and D_M were each obtained by averaging counts made on plan-view EBIC micrographs, and were supported by values determined by plan-view TEM for the samples with high densities. The mean values measured for each IJV parameter are listed along with the range in that parameter (in parentheses) which was observed for all cells on a particular wafer. Generally, the range of cell results on each epiwafer was quite small (~±3% variation in the conversion efficiency). These results demonstrate that the epitaxial growth and cell processing procedures are both under excellent control.

In the samples with $n \geq 4$, t = 8-9 µm, misfit dislocations are not present in the cell layers and the threading dislocation densities are in the mid-to-high 10^5 cm^{-2} range and are independent of the grading parameters. The SHJ solar cell IJV parameters for these samples reflect a similar independence, all showing comparable values of V_{oc}, J_{sc} and FF, giving conversion efficiencies of about 9%. This trend is consistent with the similar surface morphologies which are seen on these samples. As t is reduced to 4 µm, keeping n = 5, D_T

Table 4.4 A summary of the IJV solar cell performance parameters for $GaAs_{0.74}P_{0.26}$ shallow homojunctions (no ARC) as a function of both the grading parameters and the dislocation type and density in the junction layers. The figures in parentheses indicate the range of values observed on each device wafer.

Sample	Grading Parameters	D_T (cm^{-2})	D_M (cm^{-1})	V_{oc} (mV)	J_{sc} (mA cm^{-2})	FF (%)	η (%)
1	Continuous t = 8 μm	8×10^5	0	1244 (1233 - 1251)	8.68 (8.45 - 8.92)	84.4 (83.2 - 84.7)	9.12 (8.92 - 9.35)
2	n = 10 t = 9 μm	6×10^5	0	1230 (1212 - 1242)	8.84 (8.75 - 8.93)	83.5 (81.6 - 84.7)	9.08 (8.83-9.33)
4	n = 5 t = 8 μm	7×10^5	0	1241 (1234 - 1247)	8.33 (8.26 - 8.40)	85.8 (85.4 - 86.2)	8.87 (8.70 - 8.92)
5	n = 5 t = 4 μm	2×10^6	0	1230 (1222 - 1237)	8.00 (7.92 - 8.07)	83.2 (82.7 - 84.0)	8.19 (8.06 - 8.32)
7, 8	n = 3 t = 8 μm	2×10^6	2×10^2	666 (393 - 1051)	7.97 (7.74 - 8.16)	60.8 (50.1 - 70.4)	3.15 (2.17 - 4.90)

Table 4.4 Continued...

Sample	Grading Parameters	D_T (cm^{-2})	D_M (cm^{-1})	V_{oc} (mV)	J_{sc} (mA cm^{-2})	FF (%)	η (%)
9	n = 2 t = 8 μm	2×10^6	4×10^2	332 (328 - 336)	7.73 (7.62 - 7.86)	68.6 (68.2 - 69.4)	1.76 (1.70 - 1.80)
10	n = 1 t = 0	2×10^7	1×10^3	331 (328 - 333)	7.06 (6.93 - 7.26)	69.6 (69.3 - 69.9)	1.62 (1.59 - 1.67)

increases to $2x10^6$ cm^{-2}, resulting in a slight overall decrease in the IJV parameters and an efficiency of 8.2%. Note that the fractional loss in V_{oc} is smaller than that for J_{sc} for this increase in D_T. This result suggests that the recombination of photogenerated minority carriers at threading dislocations is the predominant loss mechanism if only threading dislocations are present. As n is reduced to 3, however, a catastrophic decrease in the cell performance is observed, presumably due to the presence of misfit dislocations in the cell layers. The cell efficiency decrease is primarily due to a sharp decline in the IJV parameters associated with the junction quality, namely V_{oc} and FF. Moreover, a wide spread in the values measured for V_{oc} and FF is also seen for the samples with n = 3. As mentioned earlier, in order to confirm the results obtained with sample 7, sample 8 was prepared in a duplicate fashion and nearly identical results were obtained. It is presumed that the extremely rough surface features on these samples in combination with the shallow n^+/p junction result in variable junction leakage from cell to cell thus resulting in the wide spread observed for these parameters. Further decreases in n and t lead to higher values of D_T and D_M and a monotonically decreasing J_{sc}, however the decline in V_{oc} and FF appears to saturate at high dislocation densities. The cell efficiencies are lowest for the sample with no compositional grading. From these data, it is clear that the presence of misfit dislocation networks in the cell layers results in a severe reduction in cell efficiency and therefore must be avoided through appropriate choice of the grading parameters. Furthermore, the trends in cell performance as a function of the grading parameters closely parallel those discussed previously for the surface morphology. Therefore, a quick visual assessment of the surface morphology can provide an accurate qualitative measure of the effectiveness of a particular compositional grade as well as the expected cell performance.

A graphical illustration of the decrease in cell efficiency due to the effects described above is shown in the IJV characteristic composite in Figure 4.10. A drastic reduction in V_{oc}

ARTHUR LAKES LIBRARY
COLORADO SCHOOL OF MINES
GOLDEN, CO 80401

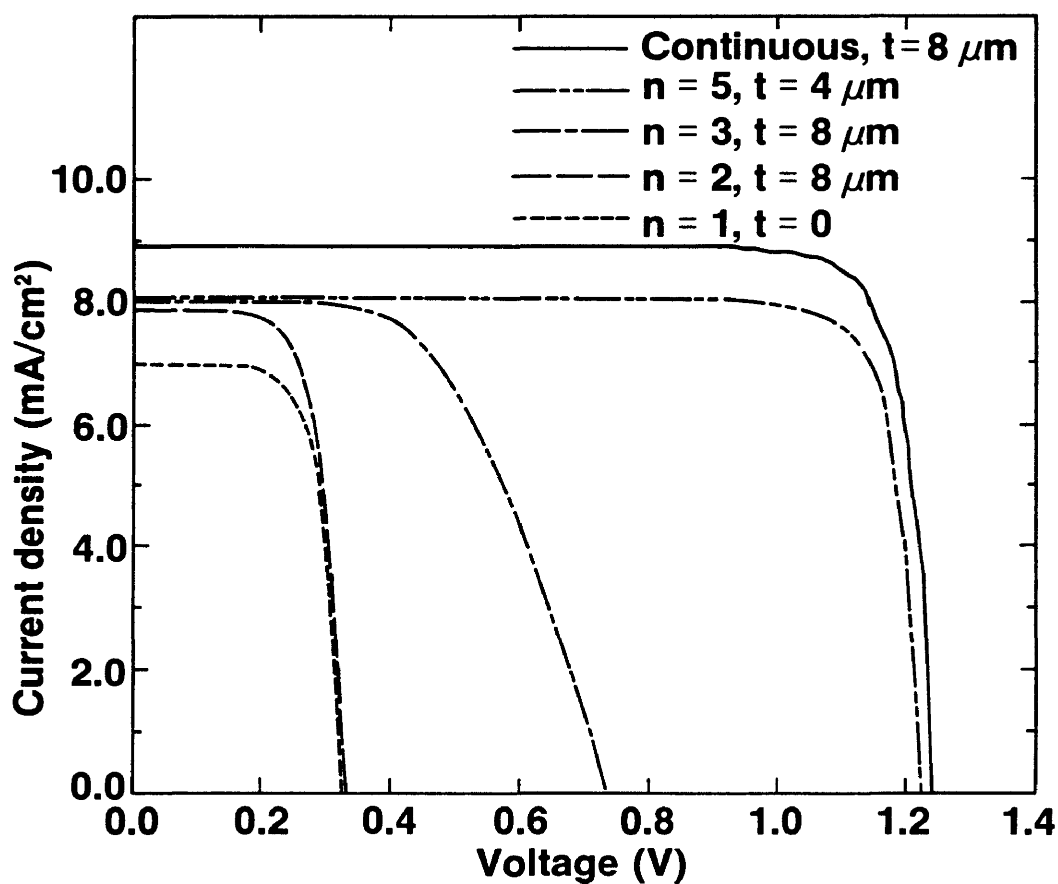

Figure 4.10 Typical J-V characteristics under standard 1-sun illumination for $GaAs_{0.74}P_{0.26}/GaAs$ SHJ solar cells (no ARC) having the five different compositionally graded structures listed.

and FF is indicated for n = 3 and below, whereas J_{sc} exhibits a smooth decrease with increasing defect density and is not affected in a severe manner by the presence of misfit dislocations.

Some interesting conclusions regarding photocurrent losses due to recombination at threading dislocations can be drawn through an analysis of the data in Table 4.4. From these data, the reduction in J_{sc} attributable to recombination at a single threading dislocation can be calculated and, therefore, the maximum tolerable density of such defects consistent with high cell efficiency can be estimated. Firstly, we consider the samples with only threading dislocations in the cell layers (i.e., samples 1, 2, 4 and 5) and assume that the loss in J_{sc} per dislocation is independent of D_T. For samples 1, 2 and 4, D_T is approximately the same for each (~7x10^5 cm^{-2}), and is roughly one third the value measured for sample 5 (2x10^6 cm^{-2}). Using the J_{sc} data for these samples, the following system of equations can be written

$$\langle J_{sc} \rangle (1,2,4) = J_{sc}(0) - J' \qquad 4.5$$

and

$$J_{sc}(5) = J_{sc}(0) - \left[\frac{D_T(5)}{\langle D_T \rangle (1,2,4)} \right] J' \qquad 4.6$$

where $\langle J_{sc} \rangle(1, 2, 4) = 8.62$ mAcm^{-2} is the average short-circuit current density for samples 1, 2 and 4, $J_{sc}(5) = 8.00$ mAcm^{-2} is the short-circuit current density for sample 5, $J_{sc}(0)$ is the short-circuit current density for the cells with no threading dislocations present, J' is the average photocurrent density lost to recombination in samples 1, 2 and 4, $D_T(5) = 2\text{x}10^6$ cm^{-2} is the threading dislocation density in sample 5 and $\langle D_T \rangle(1, 2, 4) = 7\text{x}10^5$ cm^{-2} is the average threading dislocation density in samples 1, 2 and 4. Solving the system of equations for the unknown parameters J' and $J_{sc}(0)$ yields J' = 0.33 mAcm^{-2} and $J_{sc}(0) = 8.95$ mAcm^{-2}. Thus,

by dividing J' by <D_T>(1, 2, 4) we obtain a photocurrent loss of 4.71×10^{-7} mA per threading dislocation. The fractional photocurrent loss for samples 1, 2 and 4 is obtained by dividing J' by $J_{sc}(0)$ which gives a value of 3.7%. With this information, we can determine the upper limit for the threading dislocation density which will result in a negligible (say, ≤ 1%) loss in photocurrent. For a 1% loss, D_T must be reduced to 1.9×10^5 cm^{-2}. This value is consistent with the target value of $D_T = 5 \times 10^5$ cm^{-2} determined in a recent modeling study by Yamaguchi *et al.* in order to achieve highly efficient, thin-film GaAs solar cells grown on Si substrates [4]. Furthermore, according to the ratio of J' to $J_{sc}(0)$, the effective recombination area presented by a single threading dislocation in plan view is equal to 5.29×10^{-8} cm^2 which corresponds to an effective recombination radius of 1.3 μm. This value is substantially larger than the radius of the depletion region surrounding a threading dislocation core. In a recent modeling study of GaAs solar cells grown on Si substrates, Zolper *et al.* [37] calculated that the radius of the electrically inverted cylinder around a threading dislocation is approximately 0.022 μm. The above results suggest that the diffusion of minority carriers to threading dislocations plays an important role in the recombination process. Indeed, Roedel *et al.* [23] have shown that the fractional loss of minority carriers at threading dislocations increases as the bulk minority carrier diffusion length increases.

4.3.2 Absolute External Quantum Efficiency

A composite of AEQE data for representative cells as a function of the grading parameters is shown in Figure 4.11, with the data exhibiting several noteworthy features. The high, uniform long-wavelength response for the sample with n = 10, t = 9 μm indicates that the minority carrier diffusion length is long (i.e., comparable to the base layer thickness). Similar results were obtained for other samples with n ≥ 4, t ≥ 8 μm. Overall, the quantum efficiency drops as the grading parameters become coarser. This observation is consistent with the

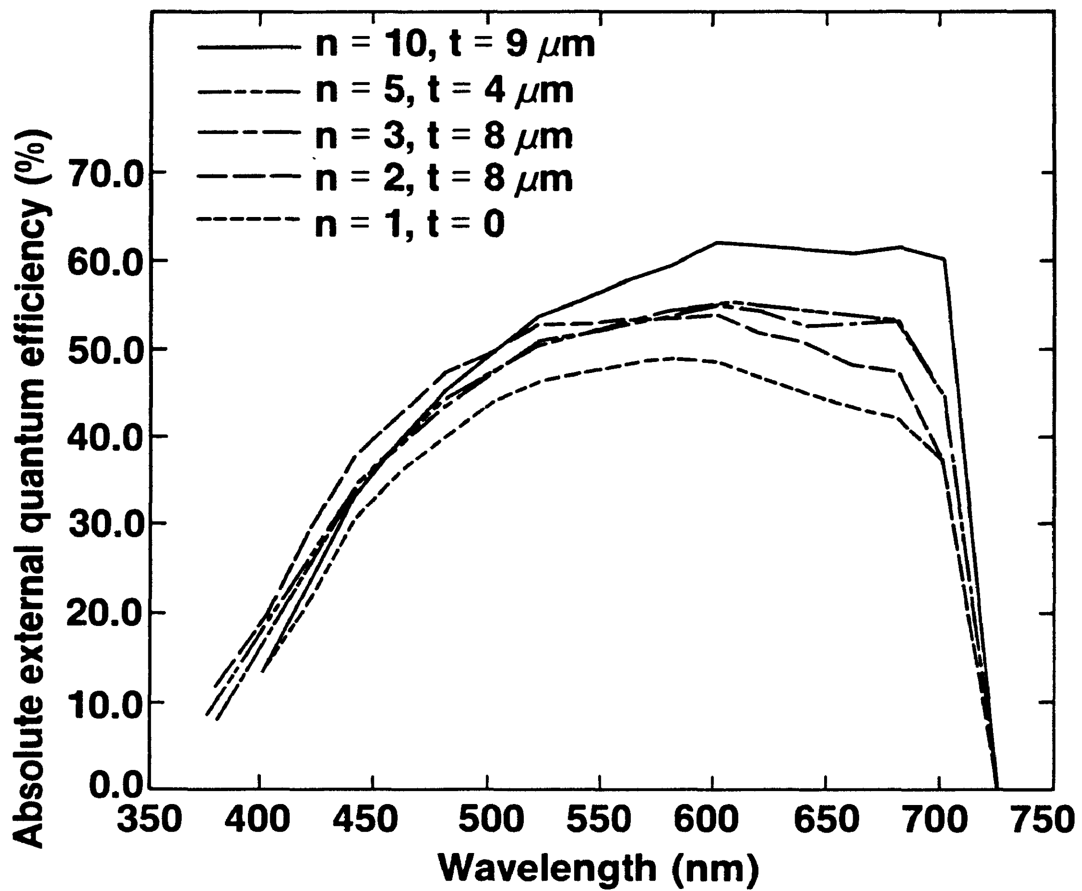

Figure 4.11 AEQE *vs* Wavelength data (no ARC) for $GaAs_{0.74}P_{0.26}$/GaAs SHJ solar cells having the five different compositional grades listed.

higher defect densities and lower values of J_{sc} measured for cells with more coarsely graded layers. In particular, the near-bandedge response shows a monotonic decrease with higher defect densities indicating that the effective minority carrier diffusion length in the p-type base layer is decreasing. The strong decrease overall in the AEQE for higher defect densities suggests that photogenerated carrier recombination occurs throughout the active cell layers.

The roll-off in short-wavelength response for these cells is typical of what is observed for SHJ cells fabricated in III-V materials due to substantial photocurrent losses at the unpassivated emitter surface. In these materials, high surface recombination velocities (typically 10^6-10^7 cm s^{-1}) are responsible for low blue response because higher energy photons have higher absorption coefficients and, therefore, a substantial fraction are absorbed in the thin emitter layer where recombination at the surface is likely to occur. Thus, the blue response is roughly independent of the grading parameters since photocurrent losses due to surface recombination are far greater than losses associated with recombination at dislocations in the emitter layer.

The transformation of the cell surface morphology as n and t are reduced has a pronounced effect on the short-wavelength AEQE. From the data in Figure 4.11, it appears that the blue response improves as n is reduced, despite the fact that the defect density increases. In particular, the data for the cell with n = 2, t = 8 μm shows the effect quite dramatically. Clearly, the enhanced blue response correlates with the onset of roughness in the surface morphology as the grading parameters become coarser (i.e., for $n \leq 3$). Apparently, the cell reflectance decreases as the surface roughens, particularly at shorter wavelengths, resulting in an increased AEQE. Unfortunately, the reflectance data for each sample was not obtained, thus precluding the possibility of comparing the internal quantum efficiencies for representative cells. Nevertheless, the differences in reflectance from cell to

cell are believed to be relatively small and, therefore, should not affect the conclusions drawn from the analysis of the IJV data discussed previously.

4.3.3 Dark J-V Characteristics

Further information concerning the influence of dislocations on junction behavior can be obtained through an analysis of DJV data, both in forward and reverse bias. Parameters such as the forward-bias diode turn-on voltage, junction ideality factor and reverse-saturation current density can be derived and used to elucidate the mechanisms governing V_{oc} and FF. Due to the presence of crystalline defects in the cell layers, however, the mechanisms determining the junction characteristics are considerably more complicated than the simple minority carrier injection and depletion-region recombination processes previously discussed in section 2.0. Therefore, a detailed analysis of the DJV characteristics was considered beyond the scope of the present study and was not attempted. However, a qualitative/semi-quantitative approach which correlates the DJV and IJV data sets has been used.

Forward-bias DJV data for representative cells as a function of different grading parameters is shown in Figure 4.12. The data clearly show that the the junction turn-on voltage is relatively constant for n > 5 and then decreases dramatically as n is reduced to 3 and below. This behavior is consistent with the catastrophic drop in V_{oc} and FF observed previously for identical variations in n. It is concluded from these results that misfit dislocations in the junction region cause a substantial decrease in the effective built-in potential of the junction thereby leading to significantly reduced values of V_{oc} and FF. Additionally, from these data the junction ideality factor and reverse-saturation current density were calculated for each cell over a voltage range in the vicinity of V_{oc}. For samples

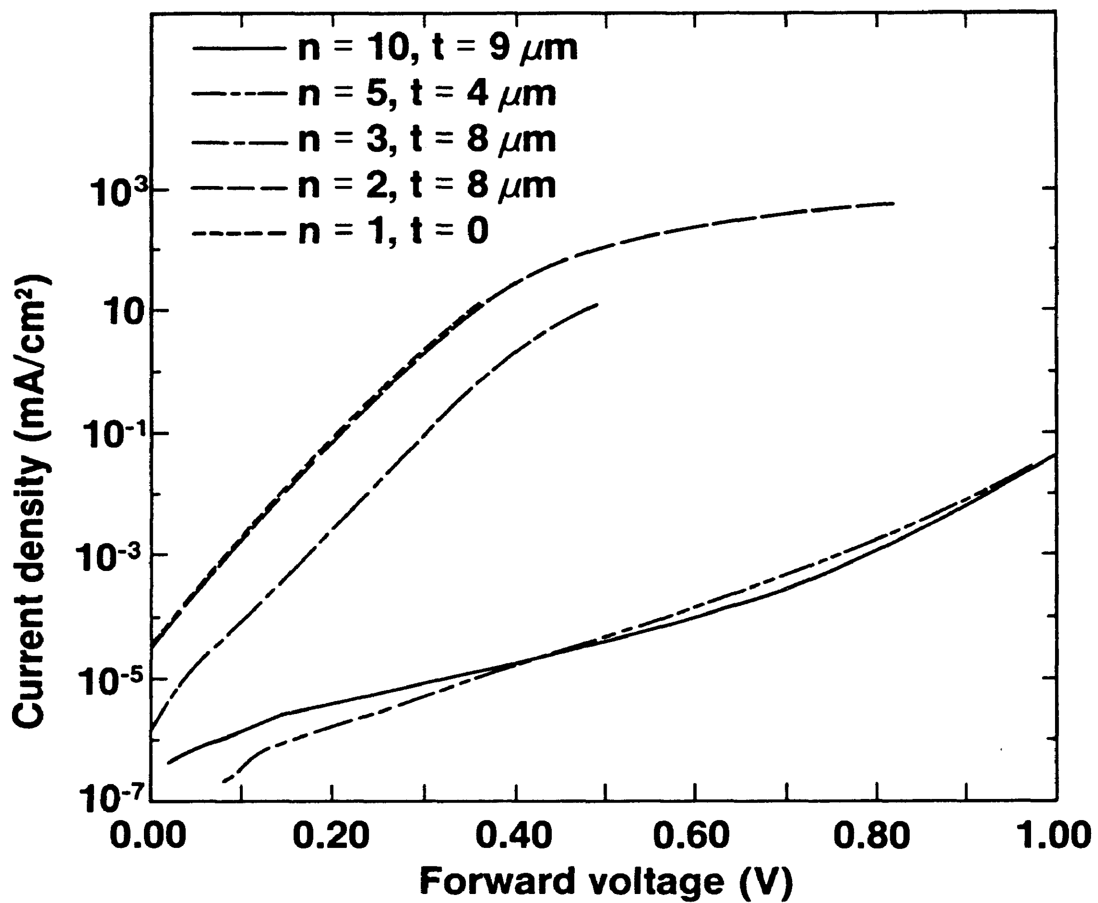

Figure 4.12 Typical forward-biased log_{10}J-V characteristics in the dark for $Ga_{0.74}P_{0.26}$/GaAs SHJ solar cells with five different compositional grades.

with $n \geq 5$, F ranges from about 1.6 to 2.2 which indicates that significant recombination in the depletion region is occuring. This suggests that threading dislocations provide a high density of mid-bandgap states through which efficient recombination proceeds. The reverse-saturation current density for these samples fell in the 10^{-10}-10^{-8} $mAcm^{-2}$ range. As n is reduced to 3 and below, F was found to lie from 1.1 to 2.4, however, the reverse-saturation current density was generally in the 10^{-5}-10^{-3} $mAcm^{-2}$ range. Thus, it is apparent that misfit dislocations are responsible for an increase in the reverse-saturation current density of about five orders of magnitude.

A DJV data composite for the same samples under reverse bias is given in Figure 4.13. Once again, the transition from low to high reverse-bias junction leakage currents occurs for $n = 3$. These data further illustrate the striking reduction in the effective junction potential attributable to misfit dislocation networks in the junction region.

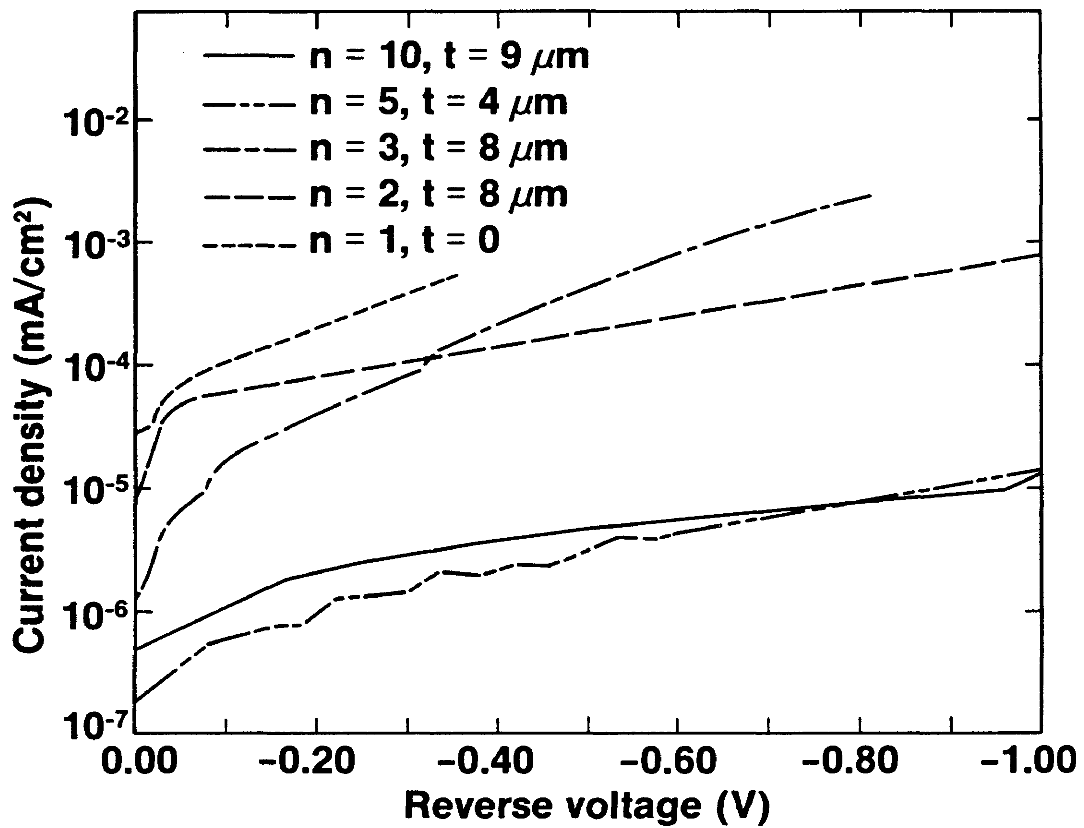

Figure 4.13 Typical reverse-biased log_{10}J-V characteristics in the dark for $GaAs_{0.74}P_{0.26}$/GaAs SHJ solar cells with five different compositional grades.

5.0 CONCLUSIONS AND SUGGESTIONS FOR FURTHER WORK

The main thrust of this research project has concerned an empirical assessment of the effects of lattice mismatch on the performance characteristics of $GaAs_{0.74}P_{0.26}$ SHJ solar cells. The project was motivated by the relevance of lattice mismatch problem to the development of high-performance tandem solar cells. However, it should be pointed out that the results of this work may have important implications, in general, for devices based on lattice mismatched heterostructures.

A compositionally graded $GaAs_{1-x}P_x/GaAs$ heterostructure epitaxially grown by APMOVPE has been employed as a means of studying the lattice mismatch problem in a controlled and systematic fashion. Using this structure, a set of nominally identical $GaAs_{0.74}P_{0.26}$ SHJ solar cells exhibiting dislocation densities and morphologies varying over a wide range have been successfully prepared and their performance characteristics compared. The success of this work is largely due to the excellent control achieved in the epitaxial growth and device processing procedures. Several analytical techniques have been used to establish correlations between the grading parameters, defect morphology, surface morphology and solar cell electrical characteristics.

Based on the results of this work, and in accordance with the orginal project objectives outlined in section 1.0, the following conclusions are drawn:

1) Thin compositional grades ($t < 10$ μm) of the proper configuration can be used effectively in the $GaAs_{0.74}P_{0.26}/GaAs$ system to produce high-performance $GaAs_{0.74}P_{0.26}$ solar cells. Furthermore, $GaAs_{0.74}P_{0.26}$ epilayers free of microcracks can be achieved despite the fact that the layers thus formed are under considerable biaxial tension.

2) In this materials system, for t ~ 8 μm continuous grades and step grades give similar results for n sufficiently large (i.e., n ≥ 4).

3) For solar cells with only threading dislocations present in the active layers, values of D_T less than $5x10^5$ cm^{-2} do not significantly degrade solar cell performance at one-sun illumination intensity. Moreover, under these circumstances it is found that the predominant power-loss mechanism is a reduction of J_{sc} through recombination of photogenerated carriers at the threading dislocations. Based on a differential analysis of J_{sc} *vs* D_T data, the effective recombination radius of a threading dislocation was determined to be 1.3 μm.

4) A catastrophic degradation in photovoltaic performance occurs when extensive misfit dislocation networks are present in the active solar cell layers. Hence, in order to achieve high cell efficiencies misfit dislocation networks must be eliminated from the cell layers through an appropriate choice of the grading parameters.

5) Strong correlations are observed between the grading parameters, dislocation type and density, surface morphology and solar cell characteristics. Finely cross-hatched surfaces are associated with cell layers that have only threading dislocations present. A rough, irregular surface morphology indicates the presence of a dense, extensive misfit dislocation network within a few microns of the surface. Furthermore, the transition from a finely cross-hatched morphology to a rough, irregular surface coincides with a catastrophic decrease in the observed solar cell performance. Therefore, a qualitative measure of the effectiveness of a particular compositional grade can be gained by simply observing the surface morphology. This purely empirical result may be useful for determining the lower limits of G or n and t for a compositional grade in an arbitrary lattice-mismatched III-V system where little is

known about the material properties.

The parameter space associated with the lattice mismatch problem is quite large and, consequently, several important areas of research in this area have been neglected in the present work and should be considered in future efforts. Suggestions for further work include:

1) An investigation of even thinner compositional grades (i.e., $t < 5$ μm), and a comprehensive comparison of continuous grades with step grades.

2) A study of the effects of biaxial tension *vs* compression on the morphological characteristics of epilayers and the electrical behavior of defects. This will require a comparison of different compositionally graded materials systems, one in tension and one in compression, but with similar values of lattice mismatch. For example, the results for cells fabricated in graded structures of $Ga_{1-x}In_xAs$ grown on GaAs substrates, thus putting the $Ga_{1-x}In_xAs$ epilayers in compression, could be compared with the present work.

3) A determination of how the solar concentration ratio affects the density of threading dislocations which can be tolerated in the cell layers. Studies have suggested that concentrator solar cells can operate efficiently with values of D_T which are significantly higher than the upper limit determined in this work for efficient one-sun operation.

4) Additional theoretical modeling studies of lattice-mismatched systems should be pursued, compared with experimental results, refined and applied to new problems and device concepts involving such systems. In this way, the full potential of lattice-mismatched heterostructures can be realized.

REFERENCES

1. E. D. Jackson, "Areas for Improvement of the Semiconductor Solar Energy Converter," Trans. Conf. on the Use of Solar Energy, Tucson, 1955, University of Arizona Press, Tucson **5** (1958) 122.

2. M. W. Wanlass, K. A. Emery, T. A. Gessert, G. S. Horner, C. R. Osterwald and T. J. Coutts, Solar Cells **27** (1989) 191.

3. L. M. Fraas, in "Current Topics in Photovoltaics," Ch. 4, (Academic Press, New York, 1985), 169.

4. M. Yamaguchi, A. Yamamoto, and Y. Itoh, J. Appl. Phys. **59** (5) (1986) 1751.

5. A. E. Blakeslee, H. Aharoni, M. W. Wanlass, A. Kibbler, K. A. Emery and C. R. Osterwald, Proc. 18th IEEE Photovoltaic Specialists Conf., Las Vegas, NV, Oct. 1985, (IEEE New York), 146.

6. E. W. Williams and R. Hall, "Luminescence and the Light Emitting Diode," (Pergamon Press, Oxford, New York, Toronto, Sydney, Paris, Frankfurt, 1978).

7. "Landolt-Boernstein Numerical Data and Functional Relationships in Science and Technology, Vol. 17a", edited by K. H. Hellwege, (Springer, Berlin, Heidelberg, New York, 1982).

8. M. S. Abrahams, L. R. Weisberg, C. J. Buiocchi and J. Blanc, J. Mater. Sci. **4** (1969) 223.

9. R. H. Saul, J. Appl. Phys. **40** (8) (1969) 3273.

10. S. Kishino, M. Ogirima and K. Kurata, J. Electrochem. Soc. **119** (5) (1972) 617.

11. S. Mader and A. E. Blakeslee, Appl. Phys. Lett. **25** (7) (1974) 365.

12. G. H. Olsen, M. S. Abrahams, C. J. Buiocchi and T. J. Zamerowski, J. Appl. Phys.

46 (4) (1975) 1643.

13. G. H. Olsen, J. Cryst. Growth **31** (1975) 223.

14. C. Schiller and J. P. Gowers, Acta Electronica **21** (2) (1978) 167.

15. S. J. Jeng, C. M. Wayman, G. Costrini and J. J. Coleman, Mat Letters **3** (9, 10) (1985) 331.

16. A. E. Blakeslee, A. Kibbler and M. W. Wanlass, J. Appl. Phys. **60** (3) (1986) 1206.

17. M. D. Camras, N. Holonyak, Jr., K. Hess, M. J. Ludowise, W. T. Dietz and C. R. Lewis, Appl. Phys. Lett. **42** (2) (1983) 185.

18. M. W. Wanlass, T. A. Gessert, M. M. Al-Jassim, J. M. Olson and A. E. Blakeslee, Proc. 18th IEEE Photovoltaic Specialists Conf., Las Vegas, NV, Oct., 1985, (IEEE, New York), 317.

19. S. M. Vernon, S. P. Tobin, V. E. Haven, R. G. Wolfson, M. W. Wanlass and R. J. Matson, Proc. 19th IEEE Photovoltaic Specialists Conf., New Orleans, LA, May, 1987, (IEEE, New York), 108.

20. M. A. Green, "Solar Cells," Prentice-Hall series in solid state physical electronics, N. Holonyak, Jr., (ed.), (Prentice-Hall, Inc., Englewood Cliffs, NJ, 07632, 1982).

21. A. Fahrenbruch and R. Bube, "Fundamentals of Solar Cells; Photovoltaic Solar Energy Conversion," (Academic Press, New York, 1983).

22. H. J. Hovel, "Semiconductors and Semimetals, Solar Cells," Vol. 11, R. K. Willardson and A. C. Beer (eds.), (Academic Press, New York, 1975).

23. R. J. Roedel, A. R. Von Neida, R. Caruso and L. R. Dawson, J. Electrochem. Soc. **126** (1979) 637.

24. R. L. Moon, J. Appl. Phys. **51** (10) (1980) 5561.

25. M. Yamaguchi, A. Yamamoto, Y. Itoh and T. Nishioka, Proc. 19th IEEE Photovoltaic Specialists Conf., New Orleans, LA, May, 1987, (IEEE, New York), 267.

26. P. D. Dapkus, Ann. Rev. Mater. Sci. **12** (1982) 243.

27. M. J. Ludowise, J. Appl. Phys. **58** (8) (1985) R31.

28. L. M. Miller and J. J. Coleman, CRC Crit. Rev. in Sol. State and Mater. Sci. **15** (1) (1988) 1.

29. G. B. Stringfellow, J. Cryst. Growth **68** (1984) 111.

30. G. B. Stringfellow, J. Cryst. Growth **70** (1984) 133.

31. See, for example, "Organometallics for Vapor Phase Epitaxy; Literature and Product Review," available from Morton Thiokol, Inc. (Alfa Products), 152 Andover Street, Danvers, MA, 01923.

32. M. W. Wanlass, U. S. Patent No. 4,649,859, Mar. 17, 1987.

33. T. Saitoh and S. Minigawa, J. Electrochem. Soc. **120** (1973) 656.

34. M. J. Ludowise and W. T. Dietze, J. Electron. Mater. **11** (1982) 59.

35. L. Samuelson, P. Omling and H. G. Grimmeiss, J. Cryst. Growth **61** (1983) 425.

36. K. A. Emery and C. R. Osterwald, Solar Cells **17** (1986) 253.

37. J. C. Zolper and A. M. Barnett, Proc. 20th IEEE Photovoltaic Specialists Conf., Las Vegas, NV, Sept. 1988, (IEEE, New York), 678.